**Noname manuscript No.**
(will be inserted by the editor)

**C. J. Pipe · T. S. Majmudar · G. H. McKinley**

# High Shear Rate Viscometry

the date of receipt and acceptance should be inserted later

**Abstract** We investigate the use of two distinct and complementary approaches to measuring the viscometric properties of low viscosity complex fluids at high shear rates up to 80,000 $s^{-1}$. Firstly we adapt commercial controlled-stress and controlled-rate rheometers to access elevated shear rates by using parallel plate fixtures with very small gap settings (down to 30 $\mu$m). The resulting apparent viscosities are gap-dependent and systematically in error but the data can be corrected - at least for Newtonian fluids - via a simple linear gap correction originally presented by Connelly & Greener (1985). Secondly we use a microfabricated rheometer-on-a-chip to measure the steady flow curve in rectangular microchannels. The Weissenberg-Rabinowitsch-Mooney analysis is used to convert measurements of the pressure-drop/flow-rate relationship into the true wall-shear rate and the corresponding shear-rate-dependent viscosity. Microchannel measurements are presented for a range of Newtonian calibration oils, a weakly shear-thinning dilute solution of poly(ethylene oxide), a strongly shear-thinning, concentrated solution of xanthan gum and a wormlike micelle solution that exhibits shear-banding at a critical stress. Excellent agreement between the two approaches is obtained for the Newtonian calibration oils, and the relative benefits of each technique are compared and contrasted by considering the physical processes and instrumental limitations that bound the operating spaces for each device.

Hatsopoulos Microfluids Laboratory, Department of Mechanical Engineering, Massachusetts Institute of Technology, Cambridge, MA 02139, USA

## 1 Introduction

The behaviour of complex liquids at large deformation rates is relevant in many processes involving coating, spraying, lubrication and injection molding. Although both shear and extensional deformations can be important in complex flows, in this study we concentrate on the rheological behaviour in steady shearing flow. From dimensional analysis we expect $\dot{\gamma} \sim U/L$, where $U$ is a characteristic velocity difference acting over a characteristic distance $L$, indicating that to attain high shear rates it is necessary to either (a) increase $U$ or (b) decrease $L$. Large velocities can lead to high Reynolds numbers $\mathrm{Re} = \rho U L/\eta$, where $\rho$ is the density and $\eta$ the dynamic viscosity of the fluid, and loss of viscometric flow. Thus it is usual to strive to minimize $L$ and the limiting factor in accessing high shear rates is the accuracy with which flow devices or rheological test fixtures can be manufactured and aligned so that geometric perturbations remain small ($\delta L/L < 1$), even when $L$ is reduced.

Various experimental configurations have been proposed for measuring viscosity at high-shear rates including cylindrical Couette flow with narrow gaps (Merrill, 1954), torsional flow between rotating parallel plates (Connelly & Greener, 1985; Kramer *et al.*, 1987; Dontula *et al.*, 1999), flow through capillaries (Talbot, 1974; Duda *et al.*, 1988) and slits (Laun, 1983; Lodge & de Vargas, 1983; Erickson *et al.*, 2002) and impact flow between a rotating ball and plate (O'Neill & Stachowiak, 1996).

Measurements using narrow gap Couette flows between concentric cylinders and between parallel-plate fixtures have been used to measure the viscosity of Newtonian and shear-thinning liquids up to $\dot{\gamma} \sim 10^6$ s$^{-1}$ (Merrill, 1954; Kulicke & Porter, 1981; Connelly & Greener, 1985; Dontula *et al.*, 1999; Mriziq *et al.*, 2004; Davies & Stokes, 2005) using gaps $0.5\ \mu\mathrm{m} \leq H \leq 50\ \mu\mathrm{m}$. Suggestions that Newtonian fluids might show a decrease in viscosity at shear rates $\dot{\gamma} \approx 5 \times 10^4$ s$^{-1}$ presented by Ram (1961) have been re-examined by Dontula *et al.* (1999), who argue that the fall in viscosity of a glycerin-water solution at high shear rates may well be due to non-viscometric flow phenomena such as viscous heating or hydrodynamic instabilities, rather than arising from a true rate-depepndent material property.

Flows through capillaries and slit channels have also been widely used to study rheology at high shear rates (Talbot, 1974; Laun, 1983; Lodge & de Vargas, 1983; Duda *et al.*, 1988; Erickson *et al.*, 2002; Kang *et al.*, 2005) and capillary viscometry can be an extremely simple and reliable technique for measuring shear viscosities. However, to minimize the importance of non-viscometric flow at the entrance and exit of the capillary it is usual to use long capillaries which can lead to long residence times for fluid elements

in the shearing flow. Furthermore at high shear rates, an evolving thermal boundary layer resulting from viscous heating must be accounted for (Duda *et al.*, 1988).

Beyond the realm of classical rheometry, custom micro-fabricated devices have also been used to measure the rheological response of complex fluids on length scales of 1–10 $\mu$m (Dhinojwala & Granick, 1997; Mukhopadhyay & Granick, 2001; Clasen & McKinley, 2004). With advances in micro- and nano-fabrication techniques (Xia & Whitesides, 1998; Marrian & Tennant, 2003) enabling the routine and reliable manufacture of flow devices with geometric features $< 100$ $\mu$m, there has been a significant increase in studies exploiting microfluidic flow geometries for rheological characterization (Hudson *et al.*, 2004; Degré *et al.*, 2006; Guillot *et al.*, 2006; Zimmerman *et al.*, 2006), although none of these studies have addressed the response at high shear rates.

As the characteristic length scale of the geometry is decreased to $O(1$ $\mu$m), it becomes increasingly important to separate the bulk rheological response of a sample from effects due to the confining surfaces (McKenna, 2006). The issue of wall slip has been shown to be significant as very small length scales are probed but nearly all experimental evidence suggests that slip, if present, occurs over length scales 0–50 nm (Granick *et al.*, 2003; Lauga *et al.*, 2007) and is therefore usually negligible for most homogeneous fluids on the micron scale. However, apparent wall slip, caused by depletion or adhesion layers at the walls, can be detected when testing heterogeneous liquids that have distinct microstructural elements even in flows with length scales $\sim 10$ $\mu$m (Degré *et al.*, 2006; Clasen *et al.*, 2006).

Studies of strongly inertial flows through channels with characteristic depths $O(100$ $\mu$m) are reviewed by Obot (2002) who finds that, despite some reports that the transition to turbulent flow in smooth-walled microchannels can occur at Reynolds numbers as low as $\mathrm{Re} \approx 200$ (eg. Peng *et al.*, 1994), the experimental evidence so far does not support a significant decrease below the usual value for macroscale flows $\mathrm{Re} \leq 2000$.

In the present study we compare and contrast the efficacy of two devices, a conventional rotational parallel plate rheometer using sample gaps in the range $10$ $\mu$m$-500$ $\mu$m, and two microfluidic slit channels with depths of 24.6 and 50.7 $\mu$m, in order to characterize shear-dependent viscosities at deformation rates up to $10^5$ s$^{-1}$. We show that the viscometric response at high rates for fluids ranging from constant viscosity mineral oils to strongly shear-thinning polymer solutions and shear-banding micellar solutions can all be determined using these techniques. We compare the results from each device to illustrate the experimental difficulties that can be encountered in each geometry and the level of reproducibility that

can be obtained. In Section 2 we present an overview of the fluids used in this work (2.1) as well as the relevant analytical framework for the parallel plates geometry (2.2) and the microfluidic channels (2.3). In Section 3.1 we investigate the use of conventional rotational rheometers to access high deformation rates, and identify errors in zeroing the gap as a primary source of discrepancy between measured values of apparent viscosity and the true viscosity. Using Newtonian calibration oils, we then implement a calibration procedure originally presented by Connelly & Greener (1985) to evaluate the gap errors. We use the resulting gap corrections to obtain true shear rates and true viscosities from the apparent values provided by the rheometer software. In addition, we investigate two additional phenomena that can affect the viscous response at high shear rates; centrifugal stresses, and viscous heating. In Section 3.2 we proceed to investigate the viscometric response of Newtonian fluids using micro-fluidic slit channels equipped with flush mounted pressure sensors. We then investigate the response in both types of device due to highly shear-thinning liquids in Section 3.3. Finally, in Section 4, we compare and contrast the results from each device to illustrate the principal experimental difficulties associated with each geometry and the level of reproducibility that can be obtained. The material and instrumental parameters constraining the application of each device are then combined to produce operating space diagrams that can guide the effective use of each approach.

## 2 Experimental techniques

### 2.1 Test fluids

Liquids exhibiting a range of viscometric behaviours, from Newtonian to strongly shear-thinning, were investigated experimentally. Mineral oils S60 and N1000 supplied by Cannon Instrument Company (PA, USA) and marketed as constant viscosity calibration fluids for viscometers as well as a Silicone oil (DMS T25) from Gelest Inc. (PA, USA), were used to test the response of Newtonian fluids with nominally constant viscosity. Henceforth, these fluids will be referred to by the labels N1, N3 and N2, respectively, as indicated in Table 1. We also study a weakly shear-thinning solution of 0.1% poly(ethylene oxide) (PEO) in a mixture of 55% glycerol - 44.9% distilled water (supplied by Sigma Aldrich MO, USA). The PEO was polydisperse with viscosity – averaged molecular weight $M_v = 2 \times 10^6$ g/mol and the solution was prepared with gentle mixing and rolling to avoid degradation of the polymer. The aqueous PEO solution was then gently mixed with the glycerol for 5 minutes and left to stand for a further 24 hours.

**Table 1** Overview of test fluids used in the present study and relevant physical parameters at 20°C. Here $\eta_0$ is the stated viscosity in the limit of zero shear rate, $\beta$ is the thermal sensitivity (see Eq. 19), and $k$ is the thermal conductivity of the fluid.

| Fluid | $\eta_0$ [Pa s] | $\beta$ [-] | $k$ [W m$^{-1}$K$^{-1}$] | Nominal viscous behaviour |
|---|---|---|---|---|
| S60 (N1) | 0.137 | 13.5 | 0.1 | Newtonian |
| DMS T25 (N2) | 0.485 | 5.5 | 0.16 | Newtonian |
| N1000 (N3) | 2.867 | 5.6 | 0.1 | Newtonian |
| Water | 0.0010 | 6.7 | 0.5 | Newtonian |
| Glycerol-water-PEO solution ($T = 22.5$°C) | 0.0155 | . | 0.4 | Weakly shear-thinning |
| Aqueous xanthan gum solution ($T = 22$°C) | 11.5 | . | . | Strongly shear-thinning |
| CPyCl/NaSal micellar solution($T = 22$°C) | 14.5 | . | . | Shear-banding |

More complex viscometric responses were explored using a strongly shear-thinning aqueous solution of 0.3% xanthan gum (Milas *et al.*, 1990) supplied by CP Kelco (GA, USA) as well as a wormlike micellar solution of 3.2 wt%/0.76 wt% cetylpyridinium chloride/sodium salicylate in 0.56 wt% sodium chloride brine (Pipe *et al.*, to be submitted) which exhibits shear-banding behaviour above a certain critical shear rate $\dot{\gamma} \approx 1$ s$^{-1}$.

## 2.2 Parallel plate apparatus and gap error correction

The rheological response of the Newtonian and non-Newtonian fluids were measured using parallel plate fixtures on an ARES strain controlled rheometer (TA Instruments, New Castle DE, USA), and an ARG2 stress controlled rheometer (TA instruments, New Castle DE, USA). In figure 1(a) we show the typical idealized arrangement assumed to exist with a parallel plate geometry. The arrangement consists of two plates of radius $R$, separated by a constant and uniform gap height $H$. In the ARES, the top plate is fixed and attached to a torque transducer, whilst the bottom plate rotates with an imposed angular velocity $\Omega$, and in the ARG2 the bottom plate is fixed and the top plate rotates under the action of an imposed torque $\mathscr{T}$. The radii of the plates on the ARES and ARG2 devices were 50 mm, and 40 mm respectively. The gap separations used in our experiments span the range from 500 down to 10 $\mu$m . In each case the temperature control is provided through the Peltier plate system, which is accurate to within $\pm 0.1$°C. In all experiments the fluid was carefully loaded between the two plates to avoid air bubbles, and the excess fluid removed to ensure a smooth cylindrical interface.

In order to accurately measure the true viscosity in rotational rheometers at narrow gaps and high shear rates, precise alignment of the parallel plates is crucial (Connelly & Greener, 1985; Kramer *et al.*, 1987). At very small gaps ($H \leq 10\ \mu$m), even the viscosity of air in the narrow gap between the plates while zeroing the gap has been noted as a possible source of error (Davies & Stokes, 2005). Here we use a calibration procedure based on the work of Connelly and Greener (Connelly & Greener, 1985) to estimate the total effective error associated with 'zeroing the gap'. Figure 1b shows the principal source of error in the alignment of plates associated with axial 'run – out' of the shaft and the resulting non – orthogonality between the plate and rotation axis. In a modern rotational rheometer using 'auto-gap zeroing' based on electrical conductivity or friction detection, the gap is considered to be 'zeroed' when any point of the top plate touches the bottom plate. A parallax in the alignment of the plates can cause the situation shown in Figure 1b, in which the gap is considered to be zero, but in reality different parts of the upper fixture are at different distances from the bottom plate. The maximum distance between the top fixture and the bottom plate sets a scale for the error incurred in zeroing the gap. This error is denoted the 'gap error' ($\epsilon$). For large gap separations ($H >> \epsilon$), this error is expected to be negligible but it is of increasing importance for small gaps. The final configuration with fluid filled between the plates is shown in Figure 1c, where the the gap is small enough ($H \sim \epsilon$) that the effect of plate misalignment is noticeable in the fluid sample confined within the plates. The analogous problem has been considered analytically for the cone-and-plate rheometer by Dudgeon & Wedgewood cite[] using a domain perturbation approach. Because the measured rheological quantities of interest such as shear rate and viscosity are dependent on the gap height, the gap error introduces a systematic error in measured quantities in addition to the intrinsic instrument accuracy.

Torque, displacement, and normal force are the fundamental quantities measured by the rheometer. These raw measurements are then used to calculate stress, strain, shear rate, viscosity, and normal stress difference. To eliminate the systematic discrepancies associated with the gap error $\epsilon$ and obtain accurate values of the calculated quantities from the measured variables, it is necessary to determine the error in gap heights via calibration, and the apparent values of measured quantities then have to be corrected for this gap error.

There are several published procedures for assessing the gap error for parallel plate geometry (Connelly & Greener, 1985; Kramer *et al.*, 1987). We follow this method with a slightly modified analysis, which is presented below. The procedure consists of single point tests of a Newtonian fluid of known

viscosity under steady simple shear flow at different gaps. In the steady shear single point test on a strain controlled rheometer, for example, a shear rate and the duration for which the specified shear rate is to be applied is specified by the user, and the viscosity is measured after the specified equilibration time. We have used shear rates from 10 $s^{-1}$ to 100 $s^{-1}$ for different fluids. The specific shear rates used were chosen such that the measured torque was well above the minimum measurable torque. At the beginning of the experiment the gap is zeroed to obtain a reference datum for all subsequent measured gap heights. The fluid is then loaded and the upper plate is lowered to a specified gap height $H$, and left undisturbed for 120 s to equilibrate at the specified temperature. An 'apparent shear rate' $\dot{\gamma}_a$, and the duration of measurement is then specified in the rheometer software. The duration for which the shear rate is applied was 30 s. At the end of one single point measurement, an 'apparent viscosity' $\eta_a$ is reported by the software. The fluid is then removed, a new sample is loaded, and the procedure is repeated at a different gap height $H$. The range of specified gap heights was decreased steadily from 500$\mu$m to 10$\mu$m.

For a given plate of radius $R$, specified gap height $H$, and angular velocity $\Omega$, the apparent shear rate $\dot{\gamma}_a$ at the rim of the rotating parallel plate fixture is given by:

$$\dot{\gamma}_a = \frac{\Omega\ R}{H}. \tag{1}$$

The apparent viscosity $\eta_a$ reported by the software is computed from the definition:

$$\eta_a = \frac{< \tau >}{\dot{\gamma}_a}, \tag{2}$$

where $< \tau >$ is the expected shear stress at the rim calculated from the measured torque, $\mathscr{T}$, assuming an ideal torsional shear flow, and is given by:

$$< \tau > \equiv \frac{2\,\mathscr{T}}{\pi\,R^3} = \eta_{\text{true}}\,\dot{\gamma}_{\text{true}}, \tag{3}$$

where $\dot{\gamma}_{\text{true}}$ and $\eta_{\text{true}}$ are the true shear rate at the rim and the true viscosity, respectively. Combining Eqs. 1,2, and 3, we have,

$$\eta_a = \frac{\eta_{\text{true}}\,\dot{\gamma}_{\text{true}}}{\Omega\,R/H}. \tag{4}$$

As discussed previously, in practice, there is always some error in zeroing the gap between the plates. For errors of the form sketched in figure 1, the gap is always biased towards larger values than the commanded

value. The simplest form of correction is to postulate (Connelly & Greener, 1985) that $H \rightarrow (H + \epsilon)$ so that the true shear rate at the rim is

$$\dot{\gamma}_{\text{true}} = \frac{\Omega R}{(H + \epsilon)}. \tag{5}$$

Combining Eqs. 4 & 5, we can write (Kramer *et al.*, 1987):

$$\frac{1}{\eta_{\text{a}}} = \frac{1}{\eta_{\text{true}}} \left\{ 1 + \frac{\epsilon}{H} \right\}. \tag{6}$$

Equation 6 suggests that for a constant gap error $\epsilon$, the reciprocal of the 'apparent' or reported viscosity $1/\eta_{\text{a}}$ should increase linearly with $1/H$. A linear regression of the apparent viscosity $\eta_{\text{a}}$ for various gap heights $H$ provides us with two relevant quantities: the intercept of the line gives $1/\eta_{\text{true}}$ and the slope gives $\epsilon/\eta_{\text{true}}$, enabling us to calculate the gap error $\epsilon$. The analysis for a stress controlled rheometer is analogous, with the same resulting relation between the true viscosity, and the commanded gap. We utilize this analysis in conjunction with gap calibration experiments on the ARES and ARG2 rheometers to obtain typical values of the gap errors for both instruments, when using parallel-plate geometries. We use the values of gap errors and Eqs. 1–6 to obtain true shear rates and true viscosities from the apparent values reported by the software. For non-Newtonian fluids in a parallel plate geometry we note that the correction to viscosity resulting from shear-thinning leads to (Bird *et al.*, 1987):

$$\eta_{\text{a}} = \frac{(\mathscr{T}/2\pi R^3)}{\dot{\gamma}_{\text{a}}} \left[ 3 + \frac{d \ln(\mathscr{T}/2\pi R^3)}{d \ln \dot{\gamma}_{\text{a}}} \right]. \tag{7}$$

Equation 7 gives the correction to viscosity due to inhomogeneity of the shear rate in a torsional flow between parallel plates. For Newtonian liquids, the logarithmic derivative term has a value of unity, thus simplifying to Eq. 2. However, for non-Newtonian fluids, the logarithmic gradient term can be different from 1, and can change the value of measured viscosity by up to 25%. In Section 3.1 we present calibration experiments using Newtonian mineral oils, implement the gap error correction analysis outlined above, and compare the results with independent measurements obtained using the microfluidic viscometer described in the next section. In Section 3.3, we present a similar analysis for non-Newtonian fluids, making use of Eq. 6 to determine gap errors and Eq. 7 to calculate shear-rate-dependent corrections to measured values of the apparent viscosities.

2.3 Microfluidic slit rheometer

The microchannels were supplied by RheoSense (VROC$^{\mathrm{TM}}$, San Ramon CA, USA) and are made from Pyrex mounted on a gold-coated silicon base containing three flush mounted MEMS pressure sensors. Figure 2 indicates the fundamental configuration of the microchannels. Values of the channel depth $d$, slit width $w$, aspect ratio $\mathscr{L} = d/w$, hydraulic diameter $d_h = 4 \times$ area/circumference and volume $\mathcal{V} = L \times w \times d$, for the two devices used in this work are given in table 2. For both slits the total channel length $L$ from inlet to outlet is 12.65 mm and the distance between the inlet and the first pressure sensor is 2.025 mm. This latter distance is equivalent to $42d_h$ and $20d_h$ for channels A and B respectively, and, for all flows considered in the present study, is significantly larger than the entrance length needed for fully developed flow: for low Reynolds numbers (where $\mathrm{Re} = \rho Q d_h/(wd\eta)$ based on the hydraulic diameter $d_h$), the entrance length is $L_e = d_h(0.6/(1 + 0.035\mathrm{Re}) + 0.056\mathrm{Re})$, and for larger Reynolds numbers before the transition to turbulence at $\mathrm{Re} \approx 2000$, $L_e = d_h(0.5 + 0.05\mathrm{Re})$ (Nguyen & Wereley, 2002). The centre-to-centre distances between the first and second pressure sensors and between the second and third sensors are 2.5 mm and 3.8 mm, respectively, resulting in pressure measurements over a total streamwise distance $L = 6.3$ mm. The MEMS pressure sensors, each measuring $800 \times 800$ $\mu$m$^2$, are located along the centre-line of the channel and were manufactured using similar techniques to those presented in Baek & Magda (2003). The maximum absolute measurable pressure $P_{\max}$ of the devices used in the present work are given in Table 2; clearly the maximum available pressure drop across the sensor array $\Delta P_{\max}$ is less than the value $P_{\max}$ in Table 2, as the latter value must also allow for additional pressure losses due to viscous stresses for the rest of the slit downstream of the final sensor before the flow exits the VROC channel at atmospheric pressure. The wet-etching process used to make the flow channels leads to rounded corners with a radius of curvature similar to the channel depth; for channel aspect ratios $\mathscr{L} \ll 1$ this deviation from a rectangular cross section is negligible. The temperature is monitored using a temperature sensor located below the silicon membrane at the centre of the channel and is accurate to within $\pm 0.25$°C.

The volume flow rate $Q$ in the channel was controlled using a PHD4400 Syringe Pump supplied by Harvard Apparatus (Holliston, MA, USA) in conjunction with Hamilton Gastight glass syringes (Reno, NV, USA) with volumes from 50 $\mu$l to 2.5 ml. Two types of tubing of varying modulus, Perfluoro alkoxy

**Table 2** Properties of VROC microchannels used in the present study (quantities are defined in the text).

| Channel | Depth $d$ [$\mu$m] | Width $w$ [mm] | Length $L$ [mm] | Aspect ratio $\mathscr{L}$ - | Hydraulic diameter $d_h$ [$\mu$m] | $P_{\max}$ [kPa] | Volume $\mathcal{V}$ [$\mu$l] |
|---|---|---|---|---|---|---|---|
| A | 24.6 | 3.1 | 12.65 | 0.0079 | 48.2 | 40 | 1.0 |
| B | 50.7 | 2.82 | 12.65 | 0.018 | 99.6 | 60 | 1.8 |

alkane (PFA; $E = 0.035$ GPa) and PEEK ($E = 3.6$ GPa), were used to connect the syringe to the VROC and no reactions were observed between the tubing and the test fluids.

Before starting the experiments the microchannel was filled with the test fluid by syringe and then left to relax so that all transients had decayed and steady state baseline pressure readings were achieved with no flow. It should be noted that for the strongly shear-thinning fluids the time necessary for pressure transients associated with the filling process to decay can be $O(1000$ s) because even small transient flow rates give rise to large viscous stresses as a result of the large zero shear viscosities of the fluids. At the beginning of each experiment, before starting the syringe pump, the pressure sensors are zeroed in the software. During experimental runs, the pressure measured by each of the sensors was monitored at 67 Hz using LabView software and each flow rate was maintained for at least 60 s to ensure that a steady state was achieved.

To find the equilibrium flow curve connecting the imposed flow rate and the measured pressure difference and hence evaluate the shear rate-dependent viscosity of a solution, the steady flow in the microchannel is considered to be a fully developed two-dimensional (2-D) flow, which is a good approximation for $\mathscr{L} \ll 1$. The pressure drop $\Delta P$ necessary to drive the flow a streamwise distance $l_0$ is related to the wall shear stress $\tau_{\rm w}$ by:

$$wd\,\Delta P = 2l_0(w+d)\tau_{\rm w}. \tag{8}$$

which represents a force balance between the pressure acting across the cross-sectional area of the channel and the viscous shear-stresses present at the walls. For incompressible 2-D flow of a constant viscosity liquid in a rectangular channel, the wall shear rate $\dot{\gamma}_{\rm w}$ is a linear function of the flow rate $Q$:

$$\dot{\gamma}_{\rm w} = \frac{6Q}{wd^2}. \tag{9}$$

For incompressible fully developed 2-D flows of liquids with a rate-dependent viscosity, the calculation of $\dot{\gamma}_{\rm w}$ is more complex because the velocity profile is no longer parabolic. Using Eq. 9 thus results in an

apparent shear rate $\dot{\gamma}_{\mathrm{a}} = 6Q/(wd^2)$ analogous to Eq. 1 obtained from the rheometer. However, because the channel dimensions are known precisely and the flow is steady and two-dimensional, the true wall shear rate can be found using the Weissenberg–Rabinowitsch–Mooney (WRM) equation (e.g. Macosko, 1994):

$$\dot{\gamma}_{\mathrm{w,true}} = \frac{\dot{\gamma}_{\mathrm{a}}}{3}\left[2 + \frac{\mathrm{d}(\ln \dot{\gamma}_{\mathrm{a}})}{\mathrm{d}(\ln \tau_{\mathrm{w}})}\right], \tag{10}$$

where $\tau_{\mathrm{w}}$ is calculated from Eq. 8. The true viscosity function is then computed as

$$\eta(\dot{\gamma}_{\mathrm{w,true}}) \equiv \frac{\tau_{\mathrm{w}}}{\dot{\gamma}_{\mathrm{w,true}}} = \frac{wd\Delta P}{2l_0(w+d)} \quad \frac{1}{\dot{\gamma}_{\mathrm{w,true}}} \tag{11}$$

It should be noted that although equation 10 is sometimes called a 'correction', it is an exact solution of the steady linear momentum equation for a generalized Newtonian fluid with a rate-dependent viscosity. To evaluate the derivative in Eq. 10, fitting the variation of $\ln \dot{\gamma}_{\mathrm{a}}(\ln \tau_{\mathrm{w}})$ with a first or second order polynomial is generally sufficient; for the wormlike micellar solution discussed below it is necessary to fit polynomials piecewise over certain ranges to capture the extreme shear-thinning behaviour observed at a critical shear-rate.

## 3 Results and Discussion

### 3.1 Parallel plates geometry: Newtonian fluids

#### *3.1.1 Gap error calibration*

We first calibrate the rheometers to quantify the gap error. In Section 2.2 it was demonstrated that the simplest gap correction model leads to a linear variation between $1/\eta_{\mathrm{a}}$ and $1/H$ (Eq. 6), and in figure 3 and figure 4. In figure 3 and figure 4 we show the gap calibration for ARES and ARG2 respectively, for three Newtonian liquids N1, N2, and N3 (with properties given in Table 1). Each fluid was subjected to steady shear for 30s, at gap heights varying from 10$\mu$m to 400$\mu$m, and apparent viscosity $\eta_a$ was calculated from the measured torque. Gap settings from 10$\mu$m to 100$\mu$m were varied in steps of 10$\mu$m, and then from 100$\mu$m to 500$\mu$m in steps of 100$\mu$m. Each data point on the plot represents the steady state value of apparent viscosity at a specific gap height. Temperatures $T$, and apparent shear rates $\dot{\gamma}_{\mathrm{a}}$ used for each fluid in the data shown is given in table 3. The solid symbols are experimental data points, and the dashed lines are fits to the data using Eq. 6, using $1/\eta_{\mathrm{true}}$ and $\epsilon$ as fitting parameters.

**Table 3** Results of gap error calibration for the three Newtonian fluids. Here $\dot{\gamma}_a$ is the apparent shear rate, $T$ is the temperature at which the fluid was maintained, $\eta_0$ is the manufacturere stated viscosity at that temperature, $\eta_{\text{true}}$ and $\epsilon$ are the true viscosity, and the size of gap error found by fitting Eq. 6 to the calibration data, respectively.

| | | ARES | | | | ARG2 | | | |
|---|---|---|---|---|---|---|---|---|---|
| Fluid | $\dot{\gamma}$ | $T$ | $\eta_0$ | $\eta_{true}$ | Gap error $\epsilon$ | $T$ | $\eta_0$ | $\eta_{true}$ | Gap error $\epsilon$ |
| | $s^{-1}$ | °C | [Pa s] | [Pa s] | [$\mu$m] | °C | [Pa s] | [Pa s] | [$\mu$m] |
| S60 (N1) | 100 | 20 | 0.137 | 0.107± 0.002 | 54 ± 1 | 25 | 0.101 | 0.120 ± 0.005 | 49 ± 2 |
| DMS T25 (N2) | 100 | 25 | 0.485 | 0.522 ± 0.004 | 27± 1 | 25 | 0.485 | 0.512 ± 0.005 | 24 ± 1 |
| N1000 (N3) | 10 | 20 | 2.867 | 2.704 ± 0.060 | 24 ± 1 | 25 | 2.01 | 2.025 ± 0.05 | 32 ± 1 |

It can be seen from the figures that all three liquids closely follow the simple linear relationship given in Eq. 6. The intercept of the straight line fit gives $1/\eta_{\text{true}}$, and the slope gives $\epsilon/\eta_{\text{true}}$. Combining the two, we calculate the measured true viscosity $\eta_{\text{true}}$, and the size of the gap error $\epsilon$. For example, for the fluid N3, fitting Eq. 6 to the data for ARES, we find:

$$\text{intercept} : \frac{1}{\eta_{\text{true}}} = 0.370 \pm 0.008 \ \text{Pa}^{-1}\text{s}^{-1}$$

$$\text{gradient} : \frac{\epsilon}{\eta_{\text{true}}} = 8.9 \pm 0.2 \ \text{m}\,\text{Pa}^{-1}\text{s}^{-1}$$

which gives $\eta_{\text{true}} = 2.70 \pm 0.060$ Pa s, and $\epsilon = 24 \pm 1$ $\mu$m, where we have propagated uncertainties in both the slope and the intercept to obtain uncertainties in the true viscosity and the gap error. The gap error obtained in this manner is a quantitative measure of the errors introduced in zeroing the gap between two plates. The results are tabulated in Table 3, where the manufacturer stated viscosity, $\eta_0$, is compared with that found from the intercept of the straight line fit to the data using Eq. 6. Also shown are the gap errors found for each case.

For the two fluids N2 and N3, the discrepancy in the stated viscosities $\eta_0$ and measured true viscosities $\eta_{\text{true}}$ are 8%, and 6%, respectively using the ARES, and 6% and 1% on ARG2, respectively. In addition, the effective gap errors obtained have values between 25–30 $\mu$m, on both rheometers. For the lowest viscosity liquid N1, the discrepancy between the stated viscosity and measured true viscosity is the largest, 21% on the ARES, and 18% on the ARG2. The gap errors obtained are also the largest, $54 \pm 1 \mu$m on ARES, and $49 \pm 2 \mu$m on ARG2. This indicates that for low viscosity fluids, there are additional sources of errors possibly due to secondary flows induced between the fixtures, which can not be captured by

**Table 4** Relative percent error in apparent viscosity and true viscosity at different gap heights $H$, assuming a representative gap error $\epsilon = 30\,\mu$m. The errors are calculated using Eq. 12.

| H [$\mu$m] | 2000 | 1000 | 500 | 100 | 50 | 30 |
|---|---|---|---|---|---|---|
| Error % | 1.5 | 3.0 | 6.0 | 30.0 | 60.0 | 100.0 |

a simple analysis of the form given in Section 2.2. The discrepancy between the value $\eta_{\text{true}}$ determined experimentally and the nominal reported value $\eta_0$ of the calibration oils provides an estimate of the accuracy of the measurements after the gap correction has been applied to the apparent viscosity $\eta_{\text{a}}$.

The apparent viscosity reported by the rheometer software is a function of both the commanded gap height $H$, and the magnitude of the gap error $\epsilon$ intrinsic to the instrument and is thus systematically in error. On rearranging Eq. 6, we find that the relative error in $\eta_{\text{a}}$ with respect to its stated value $\eta_{\text{true}}$ is given by:

$$\frac{\eta_{\text{true}} - \eta_{\text{a}}}{\eta_{\text{a}}} = \frac{\epsilon}{H} \tag{12}$$

Table 4 shows the percentage error in the true viscosity and the measured or apparent viscosity at different gap settings. It can be seen from the table that the relative percent errors increase significantly as one goes to smaller gaps; For example, assuming a representative value for the gap error to be $30\,\mu$m, at 2 mm gap height, the apparent viscosity is systematically in error by 1.5%, but at $30\,\mu$m gap height, the discrepancy is 100%. Although the fractional error between measured values of the apparent viscosity and the true viscosity can be very large at small gaps, the gap-corrected values of true viscosity using Eq. 6 fall within 10% of the stated viscosity for moderate viscosity fluids.

Ultimately the gap error determined using this approach is a composite property of the instrument and the geometry used. Using the procedure outlined above, we can estimate the size of the gap error for each instrument, and the geometric fixture used. These errors in the gap setting are not limited to Newtonian fluids, as we will demonstrate in later sections, in which we apply the same procedure for non-Newtonian fluids. The highest shear rate achievable in the instrument, $\dot{\gamma}_{\text{max}} \sim \Omega_{\text{max}} R/H$, is inversely dependent to the gap height. In any experiment there is thus a trade-off between minimizing the errors due to imperfect zeroing of the gap and the highest shear rates to be achieved. Therefore at high shear rates and small gaps, correction due to the systematic gap error become essential in obtaining accurate flow behaviour of Newtonian and complex fluids as we now proceed to demonstrate.

*3.1.2 High shear rate measurements*

In this section we describe the behaviour of Newtonian, and weakly shear thinning fluids at very high shear-rates. Even for Newtonian fluids, the issue of 'apparent shear-thinning behaviour' at high shear-rates is important (Dontula *et al.* (1999)). Do some 'Newtonian liquids' become shear thinning at high enough shear rates, or is the apparent shear-thinning behaviour explained by some other mechanism such as viscous heating. For the non-Newtonian case, particularly for worm-like micellar solutions, the high-shear rate behaviour of the solution beyond the plateau in the flow curve remains unclear (Radulescu *et al.*, 2003).

We begin by describing results for Newtonian fluids. The three Newtonian fluids N1, N2, and N3, were subjected to a steady shear ramp test on the ARES rheometer using a plate-plate geometry with plate diameter 50 mm. The fluids were subjected to shear rates from 1 $s^{-1}$ to 60000 $s^{-1}$, in logarithmic steps with 5 points per decade. Each shear step was maintained for 20 s. The commanded gap height was set to 50 $\mu$m and the temperature at the lower plate was held fixed at 25°C.

Figure 5 shows the plot of true viscosity with shear rate for the three nominally Newtonian fluids. The true viscosity and the true shear rate were obtained from the apparent values reported by the software, by correcting for the gap error, as described in Section 2.2. The gap error $\epsilon$ for the ARES rheometer was found as described in Section 3.1.1. Once the gap error was known, Eq. 5 was used to calculate true shear rate, and the gap-adjusted true viscosity using Eq. 6 in the form

$$\eta_{\text{true}} = \eta_{\text{a}} \left( \frac{H + \epsilon}{H} \right) \tag{13}$$

The solid symbols in the plot show the experimental data points. The two dashed lines running diagonally across the plot represent the minimum and the maximum limiting values of the measurable torque. The minimum and maximum torque values, for the force transducer used, are $\mathcal{T}_{\text{min}} = 1.96 \times 10^{-4}$ N m, and $\mathcal{T}_{\text{max}} = 0.196$N m, respectively. These torque limits correspond to minimum and maximum stress values $\tau_{\text{min}} = 7.989$ N/m$^2$, and $\tau_{\text{max}} = 7989$ N/m$^2$, respectively for the 50 mm diameter plate (Eq. 3). Having determined the minimum and maximum shear tresses, the range of viscosities and shear rates accessible are related by the expressions:

$$\eta_{\text{min}} = \frac{\tau_{\text{min}}}{\dot{\gamma}_{\text{true}}} \tag{14}$$

$$\eta_{\text{max}} = \frac{\tau_{\text{max}}}{\dot{\gamma}_{\text{true}}} \tag{15}$$

where the true shear rate is given by incorporating the gap error via Eq. 5.

The viscosity of each Newtonian fluid is constant for more than three decades in shear rate, up to $\dot{\gamma} \approx 10^4$ s$^{-1}$ . For the fluid N2 with viscosity $\eta_0 = 0.485$ Pa s, there is a visible drop in viscosity beyond shear rates of 20,000 $s^{-1}$. We investigate this case of apparent shear thinning in further detail below.

At very high shear rates, there are several additional factors such as inertial effects, and viscous heating that impact rheometric measurements (Bird *et al.*, 1987; Macosko, 1994). At high rotation rates, centrifugal stresses may become sufficiently large to overcome the surface tension stresses that hold the liquid between the plates resulting in liquid being thrown out of the gap; a phenomenon termed euphemistically the 'radial migration effect' (Connelly & Greener, 1985). Once the confined fluid is partially ejected, the subsequent measurements are made with less fluid within the plates, which results in a drop in measured torque, and hence in the viscosity. In particular, for a fluid with density $\rho$ and surface tension $\sigma$ in a parallel plate geometry with plate radius R, rotating with angular velocity $\Omega$, and gap height $H$ the centrifugal stresses overcome the surface tension stresses when (Tanner & Keentok, 1983; Connelly & Greener, 1985),

$$\frac{3}{20}\ \rho\ (\Omega^2 R^2) > \frac{\sigma}{H} \tag{16}$$

The critical apparent shear-rate at which the fluid begins to migrate outwards is given by rearranging Eq. 16:

$$\dot{\gamma}_{\mathrm{app,c}} = \left(\frac{\Omega R}{H}\right)_c = \sqrt{\frac{20\sigma}{3\rho H^3}} \tag{17}$$

In addition, incorporating the gap error correction, we get:

$$\dot{\gamma}_{\mathrm{c}} = \sqrt{\frac{20\sigma}{3\rho(H+\epsilon)^3}} \tag{18}$$

Equation 18 shows that the critical shear rate for radial migration to occur decreases as gap height increases ($\dot{\gamma}_{\mathrm{c}} \sim \mathrm{H}^{-3/2}$). Thus the radial migration effect can be reduced by going to very small gap heights. Furthermore, it is clear that a gap error results in a critical shear rate that is lower than the predicted critical shear rate without correcting for the gap errors. For the fluid N2 ($\eta_0 = 0.485$ Pa s), the estimated critical shear rates at which the radial migration occurs at different gap heights (assuming a gap error of 30 $\mu$m) are found to be $\dot{\gamma}_{\mathrm{c}} = 8096$ s$^{-1}$ for $H = 100$ $\mu$m, $\dot{\gamma}_{\mathrm{c}} = 16770$ s$^{-1}$ for $H = 50$ $\mu$m, and $\dot{\gamma}_{\mathrm{c}} = 29419$ s$^{-1}$ for $H = 25$ $\mu$m. It is noteworthy that these critical rates are within the range of shear rates imposed in our experiments, and of the same order as the shear rates at which the viscosity shows a noticeable drop. Many experimental and theoretical studies have shown that viscous heating

can also significantly affect the flow properties of Newtonian fluids (Bird & Turian, 1962; Connelly & Greener, 1985; Kramer *et al.*, 1987; Rothstein & McKinley, 2001; Olagunju *et al.*, 2002). In a previous study (Ram, 1961), a drop in viscosity of water/glycerol solutions was reported and described as a shear-thinning transition in an apparent Newtonian fluid at high shear rates. We re-examine this issue with fluid N2, which shows a similar drop in viscosity at high shear rates. In addition to the radial migration effect discussed above, it is possible that at very high shear rates there is sufficient viscous heating to lower the viscosity of some fluids.

The effects of viscous heating can be characterized by the Nahme number which is a dimensionless ratio of viscous heating to thermal conduction:

$$\mathrm{Na} = \frac{\eta_0 \beta H^2 \dot{\gamma}_{\mathrm{true}}^2}{kT}, \tag{19}$$

where $\eta_0$ is the zero-shear viscosity, $H$ is the true gap separation, $\dot{\gamma}_{\mathrm{true}}$ is the true shear rate, $k$ is the thermal conductivity, $T$ is the temperature, and $\beta$ is the logarithmic derivative of viscosity with temperature or "thermal sensitivity", and is given by:

$$\beta = \frac{T}{\eta_0}\left|\frac{d\eta}{dT}\right|_{T=T_0}. \tag{20}$$

At low shear rates, the Nahme number is very small ($\mathrm{Na} \sim 10^{-9}$). However, as the shear-rate increases, the Nahme number, and hence the magnitude of viscous heating increases quadratically with shear rate, and the gap height. This means that viscous heating effects become significant at lower shear rates as the gap size increases. Therefore, repeating the steady shear rate step test with different gap separations should result in noticeable difference in the viscosity-shear rate curve if viscous heating is important. Since fluid N2 shows the most noticeable decrease in viscosity at high shear rates, we perform additional tests using this fluid at gap heights of 25 $\mu$m, 50 $\mu$m and 100 $\mu$m and rotation rates corresponding to shear rates 1–60000 $\mathrm{s}^{-1}$. This range in shear rate was spanned in logarithmically spaced steps, with five points per decade, and each shear rate was maintained for a duration of 30 s. Table 5 shows the critical shear rates for the onset of radial migration effect as well as the minimum and maximum Nahme numbers for fluid N2 at three different gap heights: the use of small gaps is clearly advantageous in trying to reduce the Nahme number experienced at high shear rates and thus minimize the effects of viscous heating.

Figure 6 shows the data for the apparent viscosity versus shear rate for N2; for convenience, apparent viscosities are plotted here instead of the corrected or true viscosities, since these would collapse vertically

**Table 5** Critical shear rates for the onset of radial migration effect, and minimum and maximum Nahme numbers at different gap heights $H$, for the fluid N2

.

| $H$ [$\mu$m] | $\dot{\gamma}_c$ [s$^{-1}$] | $\mathrm{Na}_{\mathrm{min}}$ | $\mathrm{Na}_{\mathrm{max}}$ |
|---|---|---|---|
| 25 | 29400 | $8.79 \times 10^{-10}$ | 0.127 |
| 50 | 16800 | $3.52 \times 10^{-9}$ | 0.506 |
| 100 | 8100 | $1.41 \times 10^{-8}$ | 2.026 |

onto each other at low rates and obscure the onset of viscous heating. The data clearly show that the onset of apparent shear thinning occurs at different shear rates for different gap sizes, as indicated by the dashed vertical lines. Quantitatively, the shear rates at which the apparent shear thinning begins, for 100 $\mu$m, and 50 $\mu$m gap sizes are $\dot{\gamma} \approx 10^4$ s$^{-1}$ and $\dot{\gamma} \approx 2 \times 10^4$ s$^{-1}$, respectively. At the the smallest gap of 25 $\mu$m, viscous heating effects are negligible up to the maximum shear rate $\dot{\gamma} \approx 3.5 \times 10^4$ s$^{-1}$. This is consistent with the argument based on the scaling $\mathrm{Na} \sim (H\dot{\gamma})^2$: if the gap height is halved, the shear-rate necessary for the fluid to experience the same Nahme number doubles.

The first effects of viscous heating in the cone and plate geometry have been considered asymptotically by Bird and Turian (Bird & Turian, 1962; Bird *et al.*, 1987), and the analysis has been extended more recently by Olagunju (Olagunju, 2003) for parallel plate fixtures of finite radius $R$ with walls held at a constant temperature. The measured torque on the rotating plate is given by:

$$\mathscr{T} = \frac{\pi \ \mathrm{R}^3 \ \dot{\gamma}_a \ \eta_0}{2} \left[1 - \frac{Na}{18} + \mathrm{O}(Na^2) \ldots\right] \tag{21}$$

where $\dot{\gamma}_{\mathrm{a}} = \Omega R/H$. Detailed computional analysis shows that this asymptotic result is accurate for a wide range of aspect ratios up to $\mathrm{Na} \approx 1$ (Zhang & Olagunju, 2005). By combining Eqs. 19 – 21, we can calculate the shear stress and apparent viscosity at each shear rate. In figure 6 we show the predictions of the asymtotic theory (solid lines) and the data. The general trends are similar, however the decrease in viscosity observed experimentally is larger than the asymptotic theory predicts, at very high shear rates. The reasons for this may include several factors such as edge effects, the thermal variation of the thermal sensitivity $\beta(T)$, or most importantly the radial migration effect discussed above. For gap heights of 50 $\mu$m, and 100 $\mu$m, beyond a shear rate of $\dot{\gamma} \sim 10^4$ s$^{-1}$, both viscous heating and radial migration contribute synergistically to the drop in viscosity.

To confirm the presence of viscous heating, and isolate its effects from those of radial migration effect, we perform thixotropic loop tests on fluid N2, at a gap height of 50 $\mu$m following the protocol of

Connelly & Greener (1985). In this test, fluid N2 was subjected to a stepped shear ramp from 1000 $s^{-1}$ to 20000 $s^{-1}$ in logarithmic steps, and then brought back down to 1000 $s^{-1}$ in the same manner. The duration of the thixotropic loop, $t_L$, was varied from 4 s to 40 s. The maximum shear rate was chosen using Eq. 17 and Table 5 such that no significant radial migration occurs. In a thixotropic loop test, viscous heating is manifested in the form of hysteresis in the stress–strain-rate curve. If the area between the 'up' and 'down' sweeps increases with loop time, it signifies greater viscous heating due to longer duration of shearing. In figure 7, stress – strain-rate data for four different loop times $t_L = 4$ s, 10 s, 20 s, 40 s are shown. For clarity the stress values for $t_L = 10$ s, $t_L = 20$ s, and $t_L = 40$ s are shifted vertically by 500 Pa, 1000 Pa and 2000 Pa, respectively. In agreement with Connelly & Greener (1985), we observe that as the loop time is reduced, the hysteresis decreases. For the smallest loop time of 4 s viscous heating is negligible, even for a maximum imposed shear rate $\dot{\gamma} = 20000\ s^{-1}$.

To conclude, we have shown that modern rotational rheometers are capable of measuring accurate viscometric proprties at high shear rates up to $\dot{\gamma} \sim 5 \times 10^4\ s^{-1}$ provided the gap heights are kept small. Using the gap correction procedure outlined in section 2.2 accurate measurements of viscosity can be obtained at least for constant viscosity Newtonian fluids. We have also shown that the effects of viscous heating and centrifugal stresses can both be appreciable at high shear rates, and can manifest themselves as apparent shear-thinning behaviour for nominally Newtonian fluids. In view of this, we now turn to the use of micro-channel devices, which are not susceptible to the effects of either viscous heating or centrifugal stresses.

### 3.2 Rectilinear flow of Newtonian fluids in micro-channels

Fundamentally, the VROC micro-channel device allows us to measure the pressure $P(x,t)$ at various streamwise locations along the centre of a straight channel for an imposed flow rate $Q$. The steady state pressure as a function of streamwise location $x$ for fluid N1 is shown in figure 8 at three different flow rates $10 < Q \leq 50\ \mu l\,min^{-1}$. The pressure readings are sampled at 67 Hz and averaged over 10 s to show the steady-state pressure for each flow rate. Fitting a first order polynomial shows that, as one expects, for a given flow rate the streamwise pressure gradient $dP/dx$ is constant for a straight channel of uniform cross section.

The transient pressure response to a step change in flow rate is illustrated clearly in figure 9: in these tests, the fluid is initially at rest and then the syringe pump is started impulsively at time $t = 0$ s; thereafter the commanded flow rate is reduced every 60 s. The pressure is sampled at 67 Hz and the data output from the sensor software are treated with a moving average filter applied over 25 consecutive samples. The pressure drop $\Delta P$ over the array of pressure sensors as a function of time is shown for two different types of tubing, PFA (elastic modulus $E \approx 0.035$ GPa) and PEEK ($E \approx 3.6$ GPa) tubing. The residual noise of the pressure sensor is approximately $\pm 0.25\%$ full scale of the sensor, corresponding to $\pm 150$ Pa for channel B, and limiting the lowest practical working pressure drop to approximately 300 Pa where averaging over a large number of samples is required. However, much greater noise in the measured pressure can be caused by periodic fluctuations in the flow rate from the syringe pump: at 50 $\mu$l min$^{-1}$ the error is $\pm 5\%$ for the two sets of data with no bubble in the syringe. Fluctuations in flow rate can be damped significantly by introducing a compliant air bubble into the syringe and in this case the error is $\pm 1\%$. Hence it is important to average over a large number of samples to account for periodicity in the flow rate from the syringe pump.

The transient response in the pressure difference to a step change of $Q$ is clear and it is important to wait for the signal to attain a steady state in order to calculate the equilibrium values of the pressure difference $\Delta P$. This transient response is highly dependent on any air bubbles in the system as well as the viscosity of the fluid. For fluid N1 shown in figure 9, the transient pressure drop with an air bubble present is well fitted by a decaying exponential with a time constant of 3 s, while with no bubbles in the system the time constant is $< 1$ s. Therefore, to avoid long transient flows, it is important to ensure that the syringe and tubing are free of bubbles. This is critical for the shear-thinning viscoelastic liquids discussed in the following section where the time needed to reach a steady state may be $O(1000$ s) depending on the flow rate.

In figure 10 we show that the pressure difference $\Delta P$ for the three constant viscosity liquids N1, N2, and N3, is a linear function of flow rate $Q$ passing through the origin as expected. At the highest flow rate shown in figure 10, $Q = 80$ $\mu$l/min, the Reynolds number based on the hydraulic diameter of the channel is $\mathrm{Re} = \rho Q d_h/(\eta w d) = 8 \times 10^{-3}$ indicating that the flow is dominated by viscous stresses and far from the onset of any inertial effects or turbulence. The Nahme number (Eq. 19) describes the importance of viscous heating, and using the properties listed in figure 1, we find for all flow rates $\mathrm{Na} < 10^{-4}$ for fluids N1–3 indicating that viscous heating is insignificant even at the largest flow rates used in this work.

Thus we consider equations 8 & 9 for the wall shear rate and wall shear stress to provide an accurate description of the flow curve.

Viscosity data from VROC channel B for four constant viscosity fluids are shown in figure 11. The scatter in the measured value of $\eta(\dot{\gamma})$ is less than 5% and the measured viscosity is independent of shear rate as expected. As we show in table 1, the data are in good agreement with the gap–corrected measurements from the parallel-plate fixture using a standard rheometer. The upper and lower sensing limits of the VROC channel B are indicated by the dashed lines in figure 11: in the parameter space of viscosity and shear rate, a specified pressure drop $\Delta P_{\min}$ corresponds to a fixed minimum wall shear stress $(\eta\dot{\gamma})_{\min} = \tau_{\min} = wd\Delta P_{\min}/(2L(w+d))$ from Eq. 8. This corresponds to a slope of $-1$ on a log-log plot of viscosity versus shear rate. A similar analysis of course also applies for the maximum pressure drop and thus for fluids with a lower viscosity, higher shear rates can be attained.

On the same figure, we show data for water; here we can clearly see the advantage the VROC offers for low viscosity fluids, allowing shear rates $10^3 \leq \dot{\gamma} \leq 10^5$ s$^{-1}$ to be obtained for shear viscosities $\eta \sim 1$ mPa s. For these measurements the Reynolds number is in the range $1 < \mathrm{Re} < 100$ which is still significantly below the onset of turbulent flow in a channel $\mathrm{Re} = 2000$. At the maximum shear rate of $\dot{\gamma} = 8 \times 10^4$ s$^{-1}$, the Nahme number $\mathrm{Na} < 10^{-3}$ and viscous heating is negligible even at these high shear-rates.

We now proceed to investigate the viscosity of a weakly shear-thinning PEO-water-glycerol solution. In figure 12, we show data for the viscosity as a function of shear rate obtained using VROC channel A. Complementary measurements with a 60 mm diameter cone and plate fixture on an ARG2 shear rheometer show that the PEO solution has a zero shear viscosity $\eta_0 = 0.015$ Pa s at 22.5°C. With the cone and plate fixture, shear rates of up to 1000 s$^{-1}$ can be attained and the fluid exhibits slight shear-thinning for $\dot{\gamma} \gtrsim 100$ s$^{-1}$. Agreement between the viscosity measured using the cone and plate fixture and the microchannel is excellent, and using the VROC we are able to extend the shear rate range over which we can probe the viscous response to $\dot{\gamma} = 10000$ s$^{-1}$. We also indicate by the error bars the magnitude of the fluctuations in the pressure signal. At low flow rates the viscous stresses fall below the stated resolution of the VROC and there is considerable noise in the data; for example, at $\Delta P_{\min} = 55$ Pa we measure $\tau_{\min} = 0.12 \pm 0.11$ Pa.

The PEO solution is only weakly shear-thinning and in Eq. (10) the derivative term $\mathrm{d}(\ln \dot{\gamma}_\mathrm{a})/\mathrm{d}(\ln \tau_\mathrm{w}) = 1.06$, resulting in only 2% difference between $\dot{\gamma}_\mathrm{a}$ and $\dot{\gamma}_\mathrm{w}$. This error is of the same order as other experimental

errors that we would expect due to fluctuations in temperature; imposed flow rate and the precision and accuracy of the pressure transducers and it is sufficiently accurate to process the measurements for such a weakly shear-thinning fluid in the same way for a Newtonian liquid.

In summary, we have seen how streamwise pressure measurements along a straight microfluidic channel allow us to calculate the viscosity for several Newtonian liquids and weakly shear thinning-liquids over a wide range of shear rates. The measurements agree extremely well with data from a narrow gap parallel-plate geometry and have the additional advantage that no fluid is ejected from the device due to large rotation rates, and the flow remains in a low Reynolds number and low Nahme number regime.

### 3.3 Measurements of fluids with a shear-rate-dependent viscosity using parallel plates and microchannels

In Sections 3.1 & 3.2 we have demonstrated two techniques for accurately measuring the shear viscosities of Newtonian liquids at large shear rates by reducing the characteristic length scale of the device to $l \sim 30 - 50\ \mu$m. For weakly shear-thinning fluids the small shear–rate–dependent change in viscosity allows the same analysis as for a constant viscosity liquid, to within experimental error. We now extend the analysis to complex liquids with a strongly shear-rate-dependent viscosity. To investigate the possibilities and limitations of the two techniques, we present results for an aqueous xanthan gum and a CPyCl/NaSal micellar solution, which are both known *a priori* to have shear viscosities which change by several orders of magnitude over certain shear-rate ranges. The xanthan gum solution is a strongly shear-thinning liquid (Milas *et al.*, 1990) while the micellar solution shows a yield-like behaviour at a critical shear stress which is associated with the onset of shear-banding flow (Rehage & Hoffmann, 1991; Pipe *et al.*, to be submitted).

We first consider gap correction of measurements in a parallel-plate fixture with narrow gaps from $500\ \mu\text{m} - 10\ \mu$m. The method for determining the gap error and the resulting analysis to obtain true shear rates and viscosities remain the same as described in Section 2.2. In figure 13, we show gap error calibration using aqueous xanthan gum and for the CPyCl/NaSal micellar solution using the ARG2. Both fluids were subjected to steady shear for a duration of 60 s, at constant apparent shear rates of $\dot{\gamma}_\text{a} = 1\ \text{s}^{-1}$, and $\dot{\gamma}_\text{a} = 0.006\ \text{s}^{-1}$, for CPyCl/NaSal micellar solution, and xanthan gum respectively. The shear rates were chosen such that the viscometric response is expected to remain in the zero-shear rate

plateau even though the actual shear rates in the sample for small gaps may be substantially larger than the nominal values (see Table 4). The solid symbols in the plot are the experimental data, and the solid lines are linear regression fits to the data using Eq. 13, with true viscosity $1/\eta_{\text{true}}$, and size of the gap error $\epsilon$ as fitting parameters. The results of the fitting show that for xanthan gum, $\eta_{\text{true}} = 17.7 \pm 0.6$ Pa s, and $\epsilon = 31 \pm 1$ $\mu$m. For the micellar solution, $\eta_{\text{true}} = 19.1 \pm 0.4$ Pa s, and $\epsilon = 53 \pm 1$ $\mu$m. These calculated values of the viscosity at low shear rates are slightly higher but in good agreement with the zero-shear-rate viscosities given in Table 1. Although the analysis in Section 2.2 is only valid for Newtonian fluids, it also appears to apply, at least empirically, to the data in Figure 13. However interpretation of the gap error correction is complicated by the fact that it is now fluid dependent. The value of the gap error obtained with CPyCl/NaSal is much larger than the value obtained with xanthan gum solution, which is similar to that obtained for Newtonian fluids N2 and N3. Furthermore, the 'gap-correction' is found to be dependent on the imposed shear rate $\dot{\gamma}_{\text{a}}$ when higher deformation rates beyond values corresponding to the zero shear rate plateau are employed.

In particular, for the aqueous xanthan gum solution, the apparent shear rate chosen was selected to be at the edge of the constant viscosity plateau, therefore the 'true viscosity' obtained may not correspond to the zero shear-rate viscosity. The range of applicable shear rates in the case of xanthan gum is limited by the minimum measurable torque on AR-G2, which in practice is $\mathscr{T}_{\text{min}} = 1.0\,\mu$m, and the true shear rate at which shear-thinning behaviour begins, which is at $\dot{\gamma}_{\text{true}} = 0.1\,\text{s}^{-1}$. If the true shear rate falls beyond the shear-rate at which shear-thinning occurs, the analysis for gap correction needs further modification. Instead of the simple linear model for the gap error correction, corrections to the calculated viscosity due to inhomogeneity of shear-rate must also be included. Thus Eq. 6 should be modified to include variations in the shear-rate given by Eq. 7. Details of the resulting nonlinear modification to the simple linear model of gap error correction are given in Appendix A. For the shear-rates used here (close to the zero-shear-rate plateau) the additional correction is less than 5% which is within the precision of the measured data. We therefore retain the simpler linear analysis of Eq. 6.

In figure 14 the measured pressure drop $\Delta P$ is shown as a function of flow rate $Q$ for the CPyCl/NaSal and xanthan gum solutions. For both fluids $\text{d}(\ln \Delta P)/\text{d}(\ln Q) \neq 1$, indicating that the viscometric response is non-Newtonian over the range of flow rates studied. As with a constant viscosity liquid, we can still use conservation of linear momentum (Eq. 8) to relate the measured pressure drop to the wall shear stress $\tau_{\text{w}}$, but to find the true shear rate at the wall ($\dot{\gamma}_{\text{w}}$) we use equations 9 & 10. To determine

the gradient term in Eq. 10, the values of $\ln \dot{\gamma}_a = g(Q)$ evaluated from Eq. 9 are plotted as a function of $\ln \tau_w$ as shown in figure 15. Polynomial functions can be fitted to this data which can then easily be differentiated. For the strongly shear-thinning xanthan gum solution a single, second-order polynomial is sufficient, but the highly non-linear response of the micellar solution necessitates fitting polynomials piecewise to the data. At flow rates where shear-banding occurs in the CPyCl/NaSal solutions, the gradient becomes very large, i.e. the system "spurts" (Méndez-Sánchez *et al.*, 2003). Fitting a polynomial in this region leads to a large uncertainty which is reflected in subsequent calculations. However, the Newtonian–like regime at low shear rates along with the onset of shear-thinning as well as the high shear rate regime observed after the shear-banding regime is over are both well described by the respective polynomial fits. It should be noted that the value of $\mathrm{d}(\ln \dot{\gamma}_a)/\mathrm{d}(\ln \tau_w)$ is significantly different to unity for the CPyCl/NaSal and xanthan gum solutions and is therefore essential in calculating the true shear rate at the wall ($\dot{\gamma}_w$) using equation (10).

In figure 16 we show the composite steady-state flow curve for the CPyCl/NaSal solution. The measured shear stress as a function of shear rate from both micro-channels is in excellent agreement with the data measured using an ARES controlled rate rheometer. The plate-plate data from the ARES, for gap heights of 500 $\mu$m and 50 $\mu$m was first corrected for the gap error using Eq. 5, and subsequently corrected for the inhomogeneous shear rate using Eq 7. At low shear rates the Newtonian-like (constant viscosity) response and the onset of shear-thinning are captured accurately. In the steady-state stress plateau regime the error in determining the imposed shear rate, indicated by the error bars, is large as explained above because $\mathrm{d}(\ln Q)/\mathrm{d}(\ln \Delta P)$ diverges. The stress increases slowly once more after the stress plateau, and data are shown up to $\dot{\gamma} = 3000\mathrm{s}^{-1}$ for channel A and $\dot{\gamma} = 10000\mathrm{s}^{-1}$ for channel B. Cone and plate geometries which are frequently used to characterize the behaviour of micellar solutions can cause the sample to foam at high shear rates above the stress plateau due to the large viscoelastic stresses acting at the free surface. However, the micro-channels do not have a free surface in the measurement section of the channel and this allows significantly higher deformation rates to be imposed without causing foaming or incorporation of air. In this high rate region of the flow curve, the measured stress as a function of the shear rate is in good agreement between the two micro-channels; however, the results are systematically lower than the data from the plate-plate geometry. The difference between the two techniques could be due to foaming or different wetting conditions; the flow after the shear stress plateau is highly non-linear

(Pipe *et al.*, to be submitted), and the interaction of velocity fluctuations and interfacial tension may play a role in determining the flow established in this regime.

The strong monotonic shear-thinning behaviour of the xanthan gum solution is clearly illustrated in figure 17. Using a 60 mm cone and plate geometry with the controlled stress rheometer (ARG2) the zero shear viscosity and the onset of shear thinning behaviour are readily documented. Measurements with 40 mm plate-plate geometry also shows very similar behaviour. The plate-plate data was corrected for the gap as well as for the shear rate inhomogeneity using Eqs. 6, and 7. Measurements performed with VROC channel A are also able to quantify the viscosity in the shear-thinning region and capture the viscosity out to shear rates $\dot{\gamma} = 25000\text{s}^{-1}$. Here the shear-thinning behaviour begins to decrease in severity and the viscosity tends towards an infinite shear rate limit $\eta_\infty$; however, as noted by Kulicke & Porter (1981) shear-rates in excess of $10^6$ s$^{-1}$ would be required to accurately determine $\eta_\infty$. The microfluidic channel provides nearly an extra two decades of information on the shear viscosity of the xanthan gum solution. This is of considerable interest for industrial processes such as coating and spraying for which deformation rates may often approach $\dot{\gamma} \sim O(10^4$ s$^{-1})$. A Carreau-Yasuda model (Bird *et al.*, 1987) can be fitted to the complete set of cone and plate and microchannel data and describes the rate-dependent viscosity well over seven decades of shear rate.

It should be noted that the good agreement between the cone and plate and VROC measurements at high rates strongly suggests that there is no apparent wall slip present in the VROC for the aqueous xanthan gum solutions. As discussed by Degré *et al.* (2006) apparent wall slip due to depletion layers is dependent on the surface chemistry of the system as well as the ratio between the solvent and solution viscosity, and here we conclude that the hydrophilic xanthan gum polymer is not significantly repelled by the glass or gold surfaces of the microfluidic channel.

## 4 Conclusions

In this paper we have demonstrated methodologies for exploring the steady-state high-shear-rate viscous response of Newtonian and non-Newtonian fluids at high shear rates using conventional controlled stress and controlled rate rheometers as well as a new microfluidic channel-based device. For both types of device the key to accessing high shear-rates involves minimizing the length-scale over which shearing occurs.

Using the conventional rotational rheometers it is important to accurately calibrate the errors incurred in zeroing the gap when narrow gaps ($H \lesssim 250$ $\mu$m) are employed. We have demonstrated that the simple linear approach proposed by Connelly and Greener can be used to evaluate gap errors and correct the apparent viscosities obtained at different gaps to obtain true viscosities. We have implemented this approach for both Newtonian and non-Newtonian fluids, and demonstrated that the method works surprisingly well for both. We observe that for moderate viscosity Newtonian fluids N2 and N3, the true viscosities calculated via gap-calibration (Eq. 6) are within 7% of the stated zero-shear viscosities. The systematic gap offset errors obtained with these two fluids, are $\epsilon \approx 30$ $\mu$m, for both rheometers used. The lowest viscosity Newtonian fluid N1 shows significant deviation from these values. This may be due, at least partially, to larger levels of noise in the data at the lower torque limits of the instrument but it serves to remind us that this approximate gap correction approach involves both the geometry and the test fluid. In the case of non-Newtonian fluids, we have demonstrated that the same linear approximate correction works, although not uniformly well. The gap error calibration approach for the viscous aqueous xanthan gum yields values for the gap error consistent with the two Newtonian fluids N2, and N3, but the gap error obtained with a strongly shear thinning micellar solution yields higher values similar to those measured for the low viscosity Newtonian fluid N1. Thus the approach is valid for both Newtonian and non-Newtonian fluids, but with differing (and *a priori*) unknown accuracy.

We also studied the high shear-rate behaviour of Newtonian and non-Newtonian fluids. To achieve high shear rates using conventional rheometers, very small gap heights ($H < 100$ $\mu$m) must be used, leading to increased differences between the apparent viscosities and true viscosities (see Table 4), and it is essential to correct for gap errors. Using such protocols may lead to apparent shear-thinning behaviour even in Newtonian calibration oils. We identified two key systematic sources of error which could account for these observations; radial migration and viscous heating. Relevant dimensionless scalings show that both effects become important in the vicinity of shear rates $10^4$–$10^5$ s$^{-1}$.

We have also investigated the viscous response of Newtonian and non-Newtonian fluids in straight microfluidic channels. For constant viscosity liquids we are able to measure $\eta_0$ over two and a half decades of shear-rate, with the shear-rates attainable dependent on the viscosity of the fluid. For any given fluid there are resolution limits associated with the resolution of the pressure sensor, and while at the highest shear rates the percentage error is $O(\pm 0.25\%)$, the error at the very lowest shear-rates is $O(\pm 50\%)$, although this can be reduced by sampling over longer times to determine an appropriate mean value.

Additional errors in the measured steady-state viscosity can be introduced by the syringe/syringe pump set-up. To ensure that these errors are small ($< 5\%$) is is important to select a combination of syringe and syringe pump which can provide a steady and constant flow at the desired flow rate. In our experimental set-up this constraint limits measurements of high zero-shear-rate viscosity liquids at low shear rates due to the difficutly in imposing very low flow rates with sufficient accuracy. Step changes in applied flow rate lead to transient pressure drops in the microchannel and we associate this with the stiffness of the tubing between the channel and the syringe and also at the channel exit. It is especially important to reduce flow transients when using highly shear-thinning liquids and we show that a transient pressure response with a time constant $< 1$ s can be obtained by using stiff PEEK tubing.

At moderate shear rates $O(100\ \mathrm{s}^{-1})$, the measured viscosities of Newtonian calibration oils N1-3 are in excellent agreement with those obtained from conventional rheometers. Shear rates $O(10^4\ \mathrm{s}^{-1})$ can be obtained using lower zero-shear-viscosities liquids and the viscosity of water was measured up to a shear rate of $8 \times 10^4\ \mathrm{s}^{-1}$. The viscosities of two highly shear-thinning fluids calculated using the Weissenburg-Rabinowitsch-Mooney equation (Eq. 10) were also found to be in good agreement with results from cone and plate measurements and the effective shear-rate range that can be accessed is significantly increased due to the decrease in viscosity associated with increasing shear-rate. Thus we were able to characterize the viscosity of an aqueous xanthan gum solution up to $\dot{\gamma} = 30000\ \mathrm{s}^{-1}$ and capture the approach to the infinite-shear-rate viscosity. Furthermore, for a shear banding worm-like micellar liquid we have been able to explore the steady-state flow curve up to $\dot{\gamma} = 10000\ \mathrm{s}^{-1}$, charting the viscous response at shear-rates significantly beyond the end of the shear-stress plateau.

The results presented here show that both conventional rheometry, and micro-channel rheometry have their specific domains of applicability. To access high shear rates, both viscometric approaches can be used, but each has particular strengths and weaknesses. In rotational rheometers, the effects of centrifugal stresses, and viscous heating can be significant. Viscous heating effects can be substantially reduced by applying shear ramps in a very short interval of time. Radial migration effects can be mitigated by moving to very small gaps but the resulting systematic gap error grows. In addition, the magnitude of the gap correction that must be applied to the measured data appears to be dependent on the viscosity of the fluids under investigation.

Microfluidic-based rheometry offers several distinct advantages over conventional rheometry. We have demonstrated that high shear rates can be achieved using the micro-channels while still minimizing

inertial and viscous heating effects, avoiding the need for an *ad hoc* correction. On the other hand, the dynamic range of the pressure transducers mounted on the micro-channels constrains the range of fluid viscosities that can be effectively studied. For constant viscosity fluids with a zero-shear-rate viscosity upwards of 1 Pa s, the applicability of the technique is also limited by the range of flow rates that can be reached by the syringe and syringe pump set-up.

Important questions thus arise with regard to the optimal choice of rheometer for investigating the high shear-rate viscometry of a given fluid. To assess which approach is more suitable, it is helpful to have a picture of the operating space in terms of the fluid viscosities and the range of shear rates achievable for each class of device, and compare and contrast them. In Figure 18, we show the relevant operating spaces in terms of viscosity and shear rate, for a microfluidic channel (fig. 18a), and a controlled strain device (ARES) with typical fixture settings (fig. 18b). The lines 1 and 2 in figure 18a represent the lower and upper bounds for the VROC channel B based on the minimum and maximum measurable pressure difference $\Delta$P. According to Eq. 8, the measured pressure difference is directly related to the wall stress, and the apparent shear rate is directly related to the volume flow rate by Eq. 9. Thus, for the limiting values of minimum and maximum measurable pressure difference, we get:

$$\tau_{\mathrm{w,min}} = \frac{wd\Delta P_{\mathrm{min}}}{2l_0(w+d)}, \quad \tau_{\mathrm{w,max}} = \frac{wd\Delta P_{\mathrm{max}}}{2l_0(w+d)}. \tag{22}$$

Combining Eq. 22 with the relation $\tau = \eta\dot{\gamma}$ gives two limiting curves of the form:

$$\eta_{\mathrm{min}} = \frac{\tau_{\mathrm{w,min}}}{\dot{\gamma}_{\mathrm{w}}} \tag{23}$$

$$\eta_{\mathrm{max}} = \frac{\tau_{\mathrm{w,max}}}{\dot{\gamma}_{\mathrm{w}}} \tag{24}$$

These lines are power laws of slope -1 on a log-log plot. For the VROC channel B with the minimum and maximum pressure difference given in Table 2, we find $\tau_{min} = 0.8$ Pa, and $\tau_{\mathrm{max}} = 160.0$ Pa. Another important limiting case arises when the flow rate in the slit is so large that the Reynolds number for the fully developed viscous flow in the channel exceeds $\mathrm{Re} \equiv \rho Q d_h/(\eta w d) = 2000$. In this limit, the onset of turbulence results in non–viscometric flow although it should be noted that some studies in microfluidic channels (Peng *et al.*, 1994) suggest that the turbulent transition may happen considerably earlier at $\mathrm{Re} \approx 200$. Using Eq. 9, we can cast the expression for the critical Reynolds number in terms of the shear rate and viscosity relation at which Re = 2000:

$$2000 = \frac{\rho\, d_h\, d\, \dot{\gamma}_{\mathrm{w}}}{6\eta} \tag{25}$$

which gives:

$$(\dot{\gamma}_{\mathrm{w}})_{\mathrm{crit}} = \frac{12000\,\eta}{\rho\, d_h\, d}. \tag{26}$$

At the other extreme, a minimum attainable flow rate limited by the choice of syringe and the syringe pump sets a lower cut-off for the shear rate based on Eq. 9, which in this case is $\dot{\gamma}_{\mathrm{min}} = 0.014\ \mathrm{s}^{-1}$, for the minimum flow rate of $Q_{\mathrm{min}} = 1 \times 10^{-3}\ \mu\mathrm{l/min}$.

Analogously, we obtain the limiting curves, and hence operating space for a conventional rheometer such as the ARES as shown in Figure 18b. Lines 1 and 2 represent the limit curves based on the minimum and maximum measurable torques of the transducer. These limiting curves are the same as those given by Eq. 15, and are of the form $\eta_{\mathrm{min}} = \tau_{\mathrm{min}}/\dot{\gamma}$, and $\eta_{\mathrm{max}} = \tau_{\mathrm{max}}/\dot{\gamma}$. Based on the minimum and maximum torques $\mathscr{T}_{\mathrm{min}} = 1.96 \times 10^{-4}\ \mathrm{N\,m}$, and $\mathscr{T}_{\mathrm{max}} = 0.196\ \mathrm{N\,m}$, the values of the minimum and maximum shear stress are $\tau_{\mathrm{min}} = 7.989$ Pa, and $\tau_{\mathrm{max}} = 7989$ Pa for a parallel-plate fixture of radius $R = 25$ mm. Again, these are power-laws with a slope of -1. The vertical line 3 is the high shear rate cutoff at $\dot{\gamma} = 2 \times 10^4\ \mathrm{s}^{-1}$, based on the onset of radial migration (Eq. 17) and viscous heating (Eq. 19) for a typical gap height of 50 $\mu$m. As the gap spacing is increased, this limit shifts to lower shear-rates (see Eq. 18). The vertical line 4 is a low shear rate cutoff constrained by the minimum achievable rotation rate of the plate. The minimum rotation rate of the ARES motor is $\Omega = 2 \times 10^{-6}\ \mathrm{rad\,s}^{-1}$, and the minimum achievable shear rate is given by $\dot{\gamma}_{\mathrm{min}} = R\Omega_{\mathrm{min}}/H$, which for a plate of radius $R = 25$ mm, and a typical gap height $H = 50\ \mu$m, gives $\dot{\gamma}_{\mathrm{min}} = 0.001\ \mathrm{s}^{-1}$.

These operating space diagrams show the range of shear rates that can be accessed for Newtonian fluids and shear-thinning fluids of differing viscosities. For the VROC, the viscosity scale spans 7 orders of magnitude from $\eta = 10^{-5}$ Pa s to $\eta = 10^2$ Pa s, whereas for the ARES, the viscosity scale spans 9 orders of magnitude, but from $\eta = 10^{-3}$ Pa s to $\eta = 10^6$ Pa s. This points to one important difference between the two approaches: for high viscosity liquids, a conventional modern rheometer typically offers a broader dynamic range compared to the solid state pressure sensors in the microfluidic channel. For example, if the fluid has a zero shear viscosity of 10 Pa s, for the VROC the minimum and maximum shear rates applicable are $\dot{\gamma}_{\mathrm{min}} = 0.1\ \mathrm{s}^{-1}$ and $\dot{\gamma}_{\mathrm{max}} = 20\ \mathrm{s}^{-1}$, respectively, whereas using the ARES with a plate-plate fixture of radius $R = 25$ mm and gap height $H = 50\ \mu$m, the minimum and the maximum shear rates are $\dot{\gamma}_{\mathrm{min}} = 1\ \mathrm{s}^{-1}$ and $\dot{\gamma}_{\mathrm{min}} = 1000\ \mathrm{s}^{-1}$, respectively. On the other hand, inertial effects are significant for low viscosity fluids using the ARES rheometer, severely constraining the useful

range at high shear rates, while the lowest measurable torque limit curtails the accessible shear-rates at the low shear-rate end. For a fluid with zero shear viscosity of 0.001 Pa s (1 cPs), the dynamic range of shear-rate for the microfluidic device VROC is from $\dot{\gamma}_{\min} = 1000\ \text{s}^{-1}$ to $\dot{\gamma}_{\max} = 200000\ \text{s}^{-1}$, whereas for the ARES the effective range with a gap of 50 $\mu$m is from $\dot{\gamma}_{\min} = 8000\ \text{s}^{-1}$ to $\dot{\gamma}_{\max} = 20000\ \text{s}^{-1}$.

Furthermore it should be noted that the Weissenberg–Rabinowitsch–Mooney equation (Eq. 10) can be applied robustly to any pressure-flow-rate relationship obtained in the microfluidic device. By contrast, the simple linear gap correction applied to the narrow gap results for the parallel plates device is strictly applicable only to Newtonian fluid data. Our measurements suggest that a simple gap-error calibration can be applied to measurements with more complex shear thinning fluids; however, the gap offset correction $\epsilon$ is both gap- and fluid-dependent. Ideally, to confirm the applicability of the simple linear gap correction algorithm for a given fluid it is necessary to compare the gap-corrected data with a direct measure of the true shear-rate-dependent material functions, obtained for example using the microfluidic channel.

The flexibility of microfludic fabrication technologies also enables a wide range of different flow channel configurations to be considered. Having demonstrated the efficacy of a simple rectilinear slit device to determine flow curves for a range of complex fluids up to shear rates of $10^5\ \text{s}^{-1}$, we hope in the future to use this robust pressure-sensing technology to also measure entrance pressure drops and planar elongational viscosities using other rheometer-on-a-chip designs.

**Acknowledgements**

The authors would like to thank Dr. S.-G. Baek and Dr. M. Yi of Rheosense, Inc. for providing us with prototype microchannel designs. This research was supported in part by NASA (grant NNC04GA41G), NSF (DMS DMS-0406590) and a gift from the Procter and Gamble company.

## APPENDIX

In this appendix we outline the difficulties in adapting the expression for the shear-rate-dependent viscosity measured using a parallel plates device (Eq. 7):

$$\eta_{\text{true}}(\dot{\gamma}_{\text{true}}) = \frac{\mathscr{T}/2\pi R^3}{\dot{\gamma}_{\text{true}}}\left[3 + \frac{\mathrm{d}(\ln \mathscr{T}/2\pi R^3)}{\mathrm{d}(\ln \dot{\gamma}_{\text{true}})}\right], \tag{A-1}$$

to include the linear gap error analysis of Connelly and Greener. We start by noting that the analysis can follow two distinct approaches: one to find the gap error $\epsilon$ where the apparent shear rate $\dot{\gamma}_\mathrm{a}$ is held constant and the gap height $H$ is altered, and the other to find the true shear-rate-dependent viscosity where the gap height $H$ is held constant and the shear rate or rotation rate is altered.

Where possible the analysis to find the gap height error $\epsilon$ should be performed in the zero-shear-rate region so that the fluid viscosity is not a function of applied shear rate. However, for fluids which start shear-thinning at very low shear-rates this can result in measured stresses below the resolution of the rheometer torque transducer and it is not possible to access this region. In this case, we expect the apparent viscosity to be a function of both the true shear-rate and the gap setting and we want to find the gap error $\epsilon$ as a function of the apparent shear rate $\dot{\gamma}_\mathrm{a} = \Omega R/H$ which can be commanded in software. We start from expression for the the true shear-rate $\dot{\gamma}_\mathrm{true} = \Omega R/(H+\epsilon)$:

$$\dot{\gamma}_\mathrm{true} = \dot{\gamma}_\mathrm{a}\left(\frac{H}{H+\epsilon}\right), \tag{A-2}$$

and differentiating using the chain rule we find:

$$\left.\frac{\mathrm{d}\dot{\gamma}_\mathrm{true}}{\mathrm{d}\dot{\gamma}_\mathrm{a}}\right|_\Omega = \left(\frac{\partial\dot{\gamma}_\mathrm{true}}{\partial H}\right)_\Omega \frac{\mathrm{d}H}{\mathrm{d}\dot{\gamma}_\mathrm{a}} = \left(\frac{H}{H+\epsilon}\right)^2. \tag{A-3}$$

Thus we can re-write Eq. A-1 in terms of the apparent shear-rate:

$$\eta_\mathrm{true} = \frac{\mathscr{T}/2\pi R^3}{\dot{\gamma}_\mathrm{a}}\left(\frac{H+\epsilon}{H}\right)\left[3+\left(\frac{H}{H+\epsilon}\right)\left.\frac{\mathrm{d}(\ln\mathscr{T}/2\pi R^3)}{\mathrm{d}(\ln\dot{\gamma}_\mathrm{a})}\right|_\Omega\right]. \tag{A-4}$$

To solve for the gap error $\epsilon$, we cast Eq. A-4 in terms of the apparent viscosity $\eta_\mathrm{a}$ (c.f. Eq. 6):

$$\frac{1}{\eta_\mathrm{a}} = \frac{1}{\eta_\mathrm{true}}\left(1+\frac{\epsilon}{H}\right)\frac{1}{4}\left[3+\left(\frac{1}{1+\epsilon/H}\right)\left.\frac{\mathrm{d}(\ln\mathscr{T}/2\pi R^3)}{\mathrm{d}(\ln\dot{\gamma}_\mathrm{a})}\right|_\Omega\right], \tag{A-5}$$

and we note that for a complex liquid outside the zero-shear-viscosity regime $1/\eta_\mathrm{a}$ is a non-linear function of $1/H$. For a Newtonian viscous response in which $\tau \sim \dot{\gamma}_\mathrm{a}$, we recover Eq. 6 and $1/\eta_\mathrm{a}$ varies linearly with $1/H$.

We now turn to the case where we wish to determine the shear-rate-dependent viscosity as a function of the apparent shear-rate for a fixed gap height and known gap error. In this instance:

$$\left.\frac{\mathrm{d}\dot{\gamma}_\mathrm{true}}{\mathrm{d}\dot{\gamma}_\mathrm{a}}\right|_H = \left(\frac{\partial\dot{\gamma}_\mathrm{true}}{\partial\Omega}\right)_H \frac{\mathrm{d}\Omega}{\mathrm{d}\dot{\gamma}_\mathrm{a}} = \left(\frac{H}{H+\epsilon}\right), \tag{A-6}$$

and for measurements performed over a range of rotation rates at a fixed gap height, Eq. A-1 becomes (c.f. Eq. 7):

$$\eta_\mathrm{true}(\dot{\gamma}_\mathrm{true}) = \eta_\mathrm{a}\left(1+\frac{\epsilon}{H}\right)\frac{1}{4}\left[3+\left.\frac{\mathrm{d}(\ln\mathscr{T}/2\pi R^3)}{\mathrm{d}(\ln\dot{\gamma}_\mathrm{a})}\right|_H\right]. \tag{A-7}$$

It is therefore clear that for shear-thinning fluids slightly different results can be obtained depending on whether measurements are performed at constant gap (varying rotation rate) or constant rotation rate (and varying the shear-rate by changing the gap). It is instructive to compare the magnitude of the leading order correction due to (a) the error in gap height $\epsilon$ and (b) the derivative of the logarithmic term due to a shear-rate-dependent viscosity. At small gaps $H \sim 50$ $\mu$m, $\epsilon \sim 30$ $\mu$m and the correction provided by the gap correction term in Eq. A-7 can be $O(100\%)$. On the other hand, the corrections associated with the shear-thinning term in square brackets are much smaller. At low apparent shear-rates a ratio of Eq. A-5 or Eq. A-7 with the linear form of Eq. 6 in the text show that the results in Eqs. A-5 & A-7 differ by at most $[3 + (1 + \epsilon/H)^{-1}]/4$. In the case of an extremely shear-thinning fluid in which

$$\frac{\mathrm{d}(\ln \mathscr{T}/2\pi R^3)}{\mathrm{d}(\ln \dot{\gamma}_\mathrm{a})} \to 0,$$

both Eqs. A-5 & A-7 approach the same limit and the additional correction to the viscosity is only 25%. Given that the majority of fluids do not shear-thin this strongly, the additional error due to a shear-rate-dependent viscosity in many cases will be less than 10% of that due to gap-error. Thus we conclude that in the majority of experiments applying the gap-error analysis alone will provide a good estimate of the shear-rate-dependent viscosity.

## References


Baek, S. G. & Magda, J. J. 2003 Monolithic rheometer plate fabricated using silicon micromachining technology and containing miniature pressure sensors for n1 and n2 measurements. *J. Rheol.* **47** (5), 1249–1260.

Bird, R. B., Armstrong, R. C. & Hassager, O. 1987 *Dynamics of Polymeric Liquids, vol 1*, 2nd edn. John Wiley and Sons.

Bird, R. B. & Turian, R. M. 1962 Viscous heating effects in a cone and plate viscometer. *Chem. Eng. Sci.* **17** (5), 331–334.

Clasen, C., Gearing, B. P. & McKinley, G. H. 2006 The flexure-based microgap rheometer (FMR). *Journal of Rheology.* **6** (50), 883–905.

Clasen, C. & McKinley, G. H. 2004 Gap-depedent microrheometry of complex liquids. *J. Non-Newtonian Fluid Mech.* **124**, 1–10.

Connelly, R. W. & Greener, J. 1985 High-shear viscometry with a rotational parallel-disk device. *Journal of Rheology* **29** (2), 209–226.

Davies, G. A. & Stokes, J. R. 2005 On the gap error in parallel plate rheometry that arises from the presence of air when zeroing the gap. *Journal of Rheology* **49(4)**, 919–922.

Degré, G., Joseph, P. & Tabeling, P. 2006 Rheology of complex fluids by particle image velocimetry in microchannels. *Appl. Phys. Lett.* **89** (024104), 1–3.

Dhinojwala, A. & Granick, S. 1997 Micron-gap rheo-optics with parallel plates. *J. Chem. Phys.* **107** (20), 8664–8667.

Dontula, P., Macosko, C. W. & Scriven, L. E. 1999 Does the viscosity of glycerin fall at high shear rates? *Ind. Eng. Chem. Res.* **38**, 1729–1735.

Duda, J. L., Klaus, E. E. & Lin, S-C 1988 Capillary viscometry study of non-Newtonian fluids: Influence of viscous heating. *Ind. Eng. Chem. Res.* **27**, 352–361.

Erickson, D., Lu, F., Li, D., White, T. & Gao, J. 2002 An experimental investigation into the dimension-sensitive viscosity of polymer containing lubricant oils in microchannels. *Exp. Thermal Fluid Sci.* **25**, 623–630.

Granick, S., Zhu, Y. & Lee, H. 2003 Slippery questions about complex fluids flowing past solids. *Nature Materials* **2**, 221–227.

Guillot, P., Panizza, P., Joanicot, J.-B. Salmon M. & Colin, A. 2006 Viscosimeter on a microfluidic chip. *Langmuir* **22**, 6438–6445.

Hudson, S. D., Phelan, F. R., Handler, M. D., Cabral, J. T., Migler, K. B. & Amis, E. J. 2004 Microfluidic analog of the four-roll mill. *Appl. Phys. Lett.* **85** (2), 335–337.

Kang, K., Lee, L. J. & Koelling, K. W. 2005 High shear microfluidics and its application in rheological measurement. *Exp. Fluids* **38**, 222–232.

Kramer, J., Uhl, J. T. & Prud'Homme, R. K. 1987 Measurement of the viscosity of guar gum solutions to 50,000 $s^{-1}$ using a parallel plate rheometer. *Polymer Engineering and Science* **27** (8), 598–602.

Kulicke, W.-M. & Porter, R. S. 1981 High-shear viscometry of polymer solutions. *J. Polym. Sci.* **19**, 1173–1176.

Lauga, E., Brenner, M. P. & Stone, H. A. 2007 *Microfluidics: the no-slip boundary condition, Handbook of experimental fluid dynamics*. Springer.

Laun, H. M. 1983 Polymer melt rheology with a slit die. *Rheol. Acta* **22**, 171–185.

Lodge, A. S. & de Vargas, L. 1983 Positive hole pressures and negative exit pressures generated by molten polyethylene flowing through a slit die. *Rheol. Acta* **22**, 151–170.

Macosko, C. W. 1994 *Rheology: Principles, Measurements and Applications*. Wiley-VCH.

Marrian, C. R. K. & Tennant, D. M. 2003 Nanofabrication. *J. Vac. Sci. Technol. A* **21** (5), 207–215.

McKenna, G. B. 2006 Commentary on rheology of polymers in narrow gaps. *Eur. Phys. J. E* **19** (1), 101–108.

Méndez-Sánchez, A. F., Pérez-González, J., de Vargas, L., Castrejón-Pita, J. R., Castrejón-Pita, A. A. & Huelsz, G. 2003 Particle image velocimetry of the unstable capillary flow of a micellar solution. *J. Rheol.* **47** (6), 1455–1466.

Merrill 1954 A coaxial cylinder viscometer for the study of fluids under high velocity gradients. *J. Coll. Sci.* **9**, 7–19.

Milas, M., Rinaudo, M., Knipper, M. & Schuppiser, J. L. 1990 Flow and viscoelastic properties of xanthan gum solutions. *Macromolecules* **23** (9), 2506–2511.

Mriziq, K. S., Dai, H. J., Dadmun, M. D., Jellison, G. E. & Cochran, H. D. 2004 High-shear-rate optical rheometer. *Reviews of Scientific Instruments* **75** (6), 2171–2176.

Mukhopadhyay, A. & Granick, S. 2001 Micro- and nanorheology. *Curr. Opin. Colloid Interface Sci.* **6**, 423–429.

Nguyen, N.-T. & Wereley, S. T. 2002 *Fundamentals and Applications of Microfluidics*. Artech House.

Obot, N. T. 2002 Toward a better understanding of friction and heat/mass transfer in microchannels–a literature review. *Microscale Thermophys. Eng.* **6** (3), 155–173.

Olagunju, D. 2003 Analytical solutions for non-isothermal viscoelastic torsional flow in a bounded domain. *Journal of Non-Newtonian fluid Mechanics* **112**, 85–100.

Olagunju, D. O., Cook, L. P. & McKinley, G. H. 2002 Effect of viscous heating on linear stability of viscoelastic cone-and-plate flow: axisymmetric case. *Journal of Non-Newtonian Fluid Mechanics* **102**, 321–342.

O'Neill, P. L. & Stachowiak, G. W. 1996 A high shear rate, high pressure microviscometer. *Tribology Int.* **29** (7), 547–557.

Peng, X. F., Peterson, G. P. & Wang, B. X. 1994 Frictional flow characteristics of water flowing through rectangular microchannels. *Exp. Heat Transfer* **7** (4), 249 – 264.

Pipe, C. J., Kim, N. J., McKinley, G. H., Vasquez, P. A. & Cook, L. P. to be submitted Wormlike micellar solutions II: comparison between experimental data and scission model predictions. *J. Non-Newtonian Fluid Mech.* **submitted**.

Radulescu, O., D., Olmsted P., P., Decruppe J., S., Lerouge, F., Berret J. & G., Porte 2003 Time scales in shear banding of wormlike micelles. *Europhysics Letters* **62 (2)**, 230–236.

Ram, A. 1961 *High-Shear Viscometry of Polymer Solutions. Sc.D. Thesis*. Massacusetts Institute of Technology, Boston, MA.

Rehage, H. & Hoffmann, H. 1991 Viscoelastic surfactant solutions: model systems for rheological research. *Molecular Physics* **74** (5), 933–973.

Rothstein, J. & McKinley, G. H. 2001 Non-isothermal modification of purely elastic flow instabilities in torsional flows of polymeric fluids. *Physics of Fluids* **13-2**, 382–396.

Talbot, A. F. 1974 High shear viscometry of concentrated solutions of poly (alkylmethacrylate) in a petroleum lubricating oil. *Rheol. Acta* **13**, 305–317.

Tanner, R. I. & Keentok, M. 1983 Shear fracture in cone-plate rheometry. *Journal of Rheology* **27**, 47–57.

Xia, Y. & Whitesides, G. M. 1998 Soft lithography. *Annu. Rev. Mater. Sci.* **28**, 153–184.

Zhang, S. & Olagunju, D. O. 2005 Axisymmetric finite element solution of non-isothermal parallel-plate flow. *Appl. Math Comput.* **171**, 1081–1094.

Zimmerman, W. B., Rees, J. M. & Craven, T. J. 2006 Rheometry of non-Newtonian electrokinetic flow in a microchannel T-junction. *Microfluid Nanofluid* **2**, 481–492.

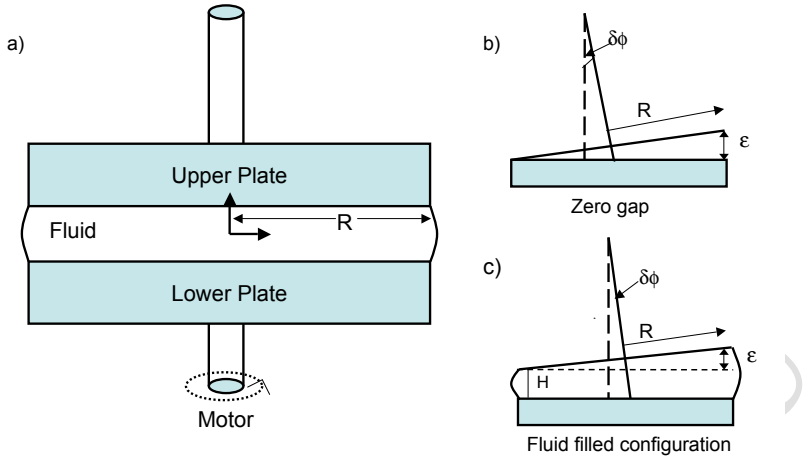


**Fig. 1** Experimental schematic: Schematic diagram of a conventional rotational rheometer; two plates of radius R, at gap height H. The top or the bottom plate rotates with an angular velocity $\Omega$. a) Ideal situation in a parallel plate rheometer, the plates are perfectly parallel. b) Sources of error during gap zeroing; a slight parallax (exaggerated in the figure) causes the plates to touch when not parallel, thus introducing a gap error of size $\epsilon$. c) profile of the fluid placed between non-parallel plates.

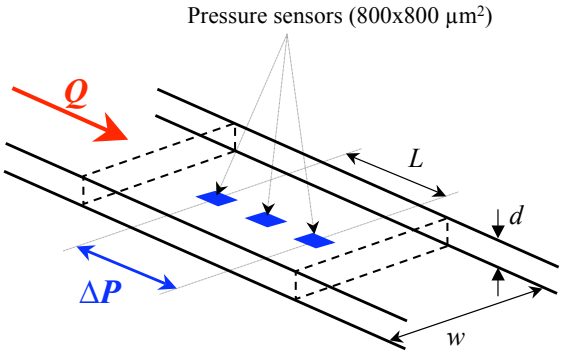


**Fig. 2** Sketch of RheoSense VROC slit micro-rheometer; the dimensions are given in the text.

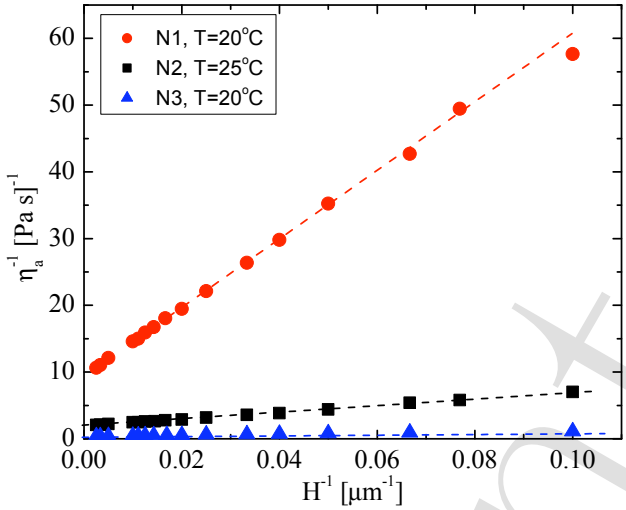


**Fig. 3** Gap error calibration data for three Newtonian fluids N1, N2, and N3, for the strain-controlled ARES rheometer. The plot shows the inverse of the apparent viscosity plotted against inverse of the gap height. The solid symbols are the experimental data, and the dashed lines show the fits of Eq. 6 to the data. The experimental parameters, and the results of the fit, the true viscosities $\eta_{\text{true}}$, and the gap errors $\epsilon$ are given in Table 3.

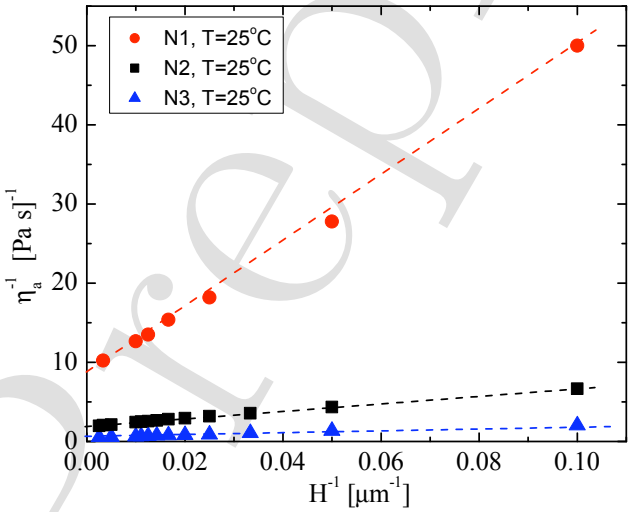


**Fig. 4** Gap error calibration data for three Newtonian fluids N1, N2, and N3, for the stress-controlled AR-G2 rheometer. The plot shows the inverse of the apparent viscosity plotted against inverse of the gap height. The solid symbols are the experimental data, and the dashed lines show the fits of Eq. 6 to the data. The experimental parameters, and the results of the fit, the true viscosities $\eta_{\text{true}}$, and the gap error $\epsilon$ are given in Table 3.

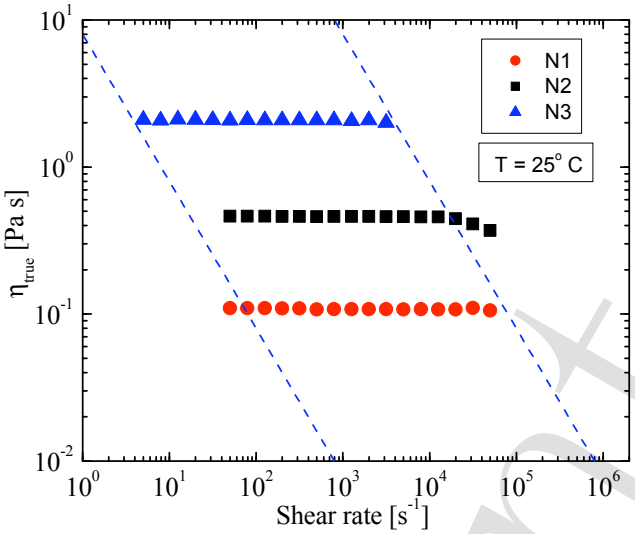


**Fig. 5** High shear rate behaviour of Newtonian fluids N1, N2, and N3 in the ARES rheometer, using 50 mm diameter parallel plate geometry at 25°C. The solid symbols are the gap-corrected or 'true' experimental data points, and the dashed lines show the limiting curves of slope -1 given by Eq. 15, based on the minimum and the maximum measurable torque values.

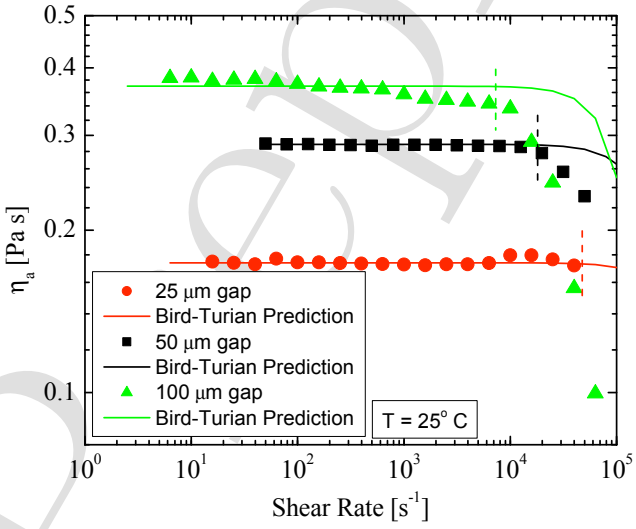


**Fig. 6** High shear behaviour of Newtonian fluid N2, at three different gap sizes, $H = 25\ \mu$m, $H = 50\ \mu$m, and $H = 100\ \mu$m. The filled symbols are the experimental data from steady shear step tests, and the lines are the *a priori* predictions of the modified Bird-Turian analysis (Eq. 21). The vertical dashed lines show the shear rates for the onset of apparent shear thinning. The minimum and the maximum Nahme numbers $\mathrm{Na_{min}}$, and $\mathrm{Na_{max}}$ corresponding to the minimum and maximum shear rates are given in Table 5.

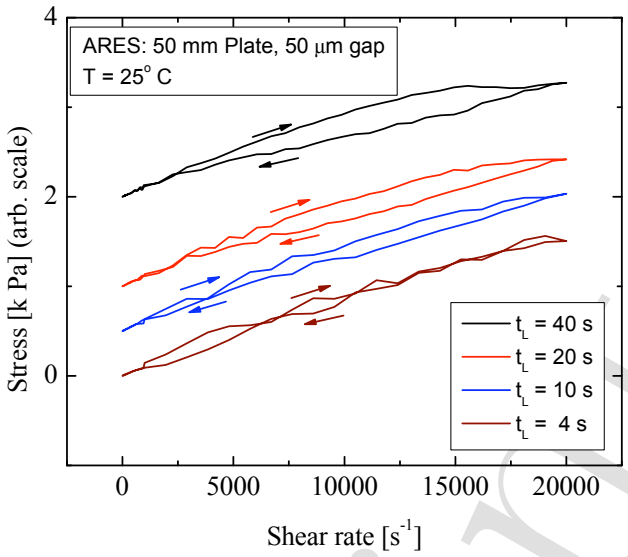


**Fig. 7** Thixotropic loops showing variation of stress with shear rate at four different loop times, $t_L = 4$ s, $t_L = 10$ s, $t_L = 20$ s, and $t_L = 40$ s. The latter three curves are shifted vertically by 500 Pa, 1000 Pa and 2000 Pa for clarity of presentation only.

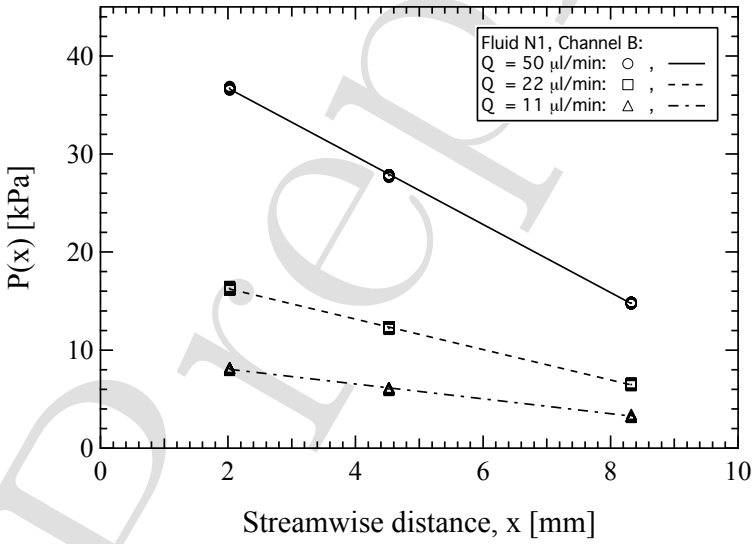


**Fig. 8** Fluid S60 in channel B, steady state pressure $P(x)$ measured at each pressure sensor for 10 s at three flow rates $Q$. The lines are a least-squares fit of a first order polynomial.

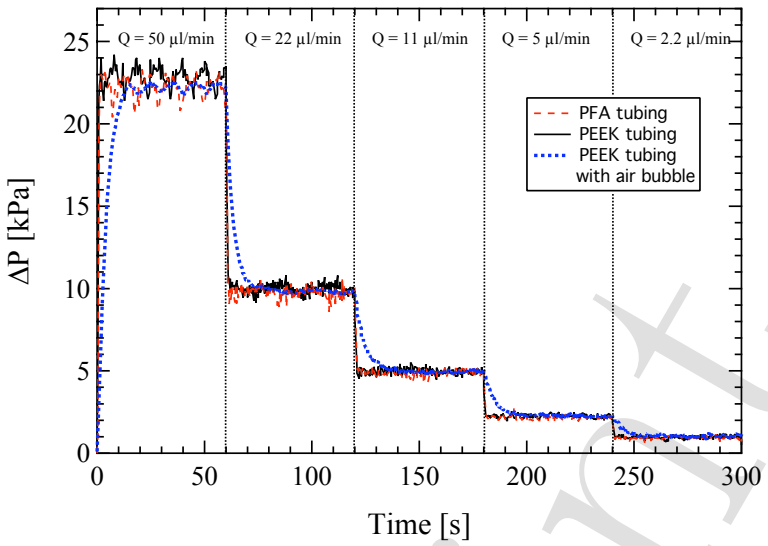


**Fig. 9** Fluid S60 in channel B, pressure drop $\Delta P$ as a function of time at several flow rates $Q$.

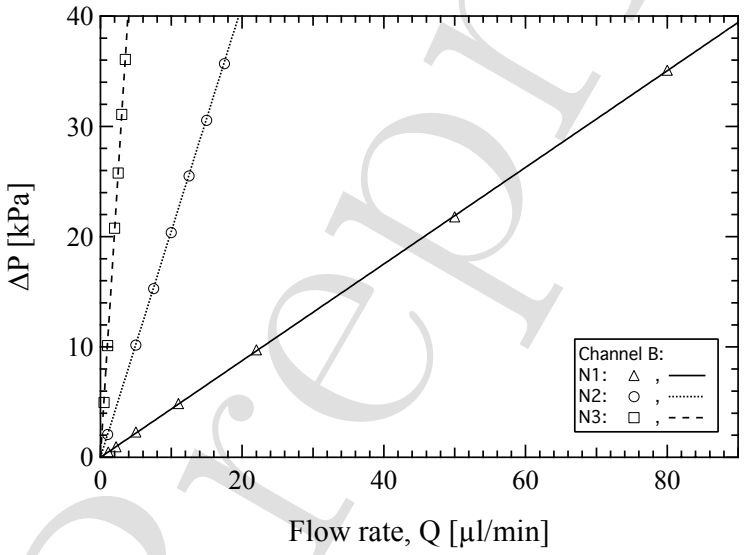


**Fig. 10** Pressure drop $\Delta P$ as a function of flow rate $Q$ in VROC channel B for Newtonian fluids N1, N2, and N3; experimental data (symbols) and linear fit (solid line).

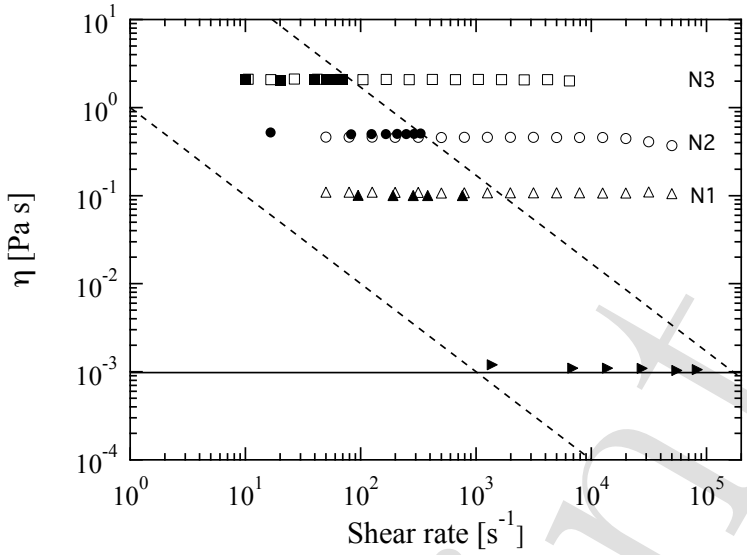


**Fig. 11** Measured viscosity as a function of shear rate for the three viscous Newtonian calibration fluids N1, N2, N3, and water. Solid symbols are for data from the VROC microchannel obtained using channel A, and hollow symbols are for data obtained using plate-plate geometry on ARES. The dashed lines show the minimum and maximum operating pressure for the microchannel.

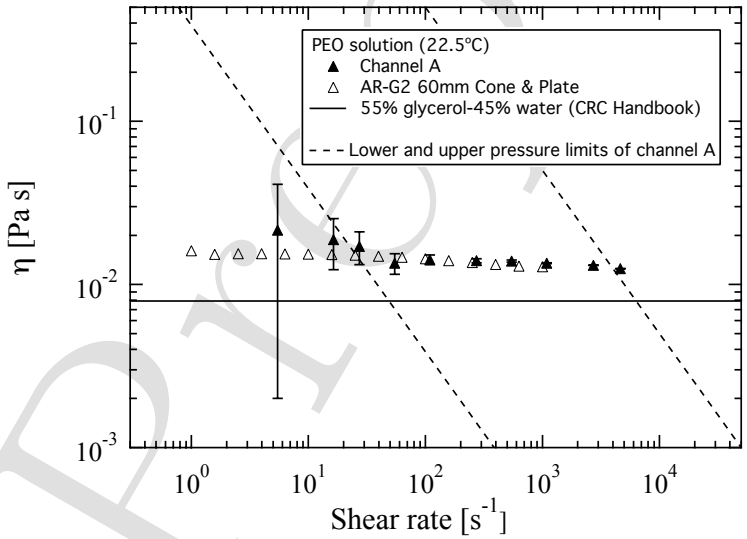


**Fig. 12** Viscosity as a function of shear rate for a shear-thinning PEO solution (55% glycerol, 44.9% water and 0.1% PEO). Data from measurements performed using VROC channel A.

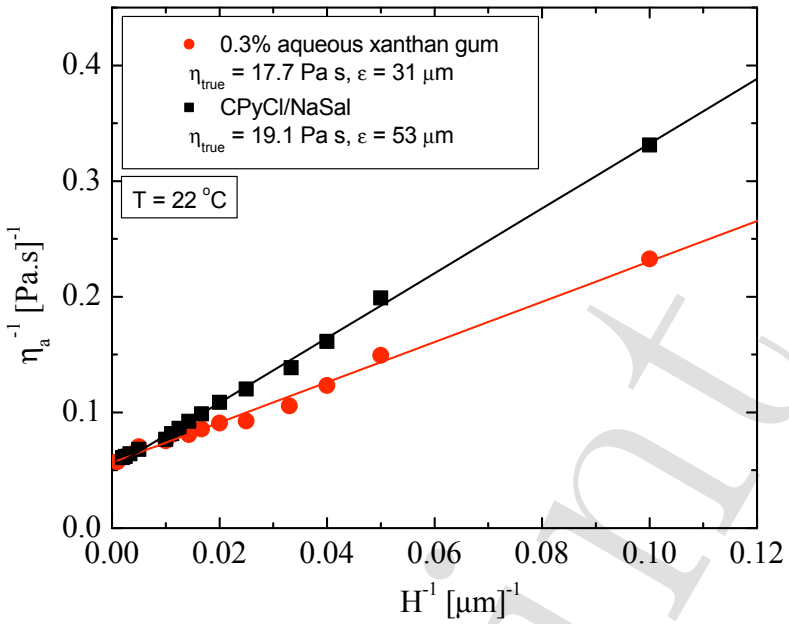


**Fig. 13** Gap error calibration data for two non-Newtonian fluids (CpyCl/NASal, and xanthan gum) on the ARG2 rheometer. The gap separations range from 10 $\mu$m to 500 $\mu$m. For CPyCl/NaSal the apparent shear rate was held constant at $\dot{\gamma}_a = 1$ s$^{-1}$, and for xanthan gum $\dot{\gamma}_a = 0.006$ s$^{-1}$. The lines are fits of Eq. 6 to the data and the errors in the least squares linear fit are reported in the text.

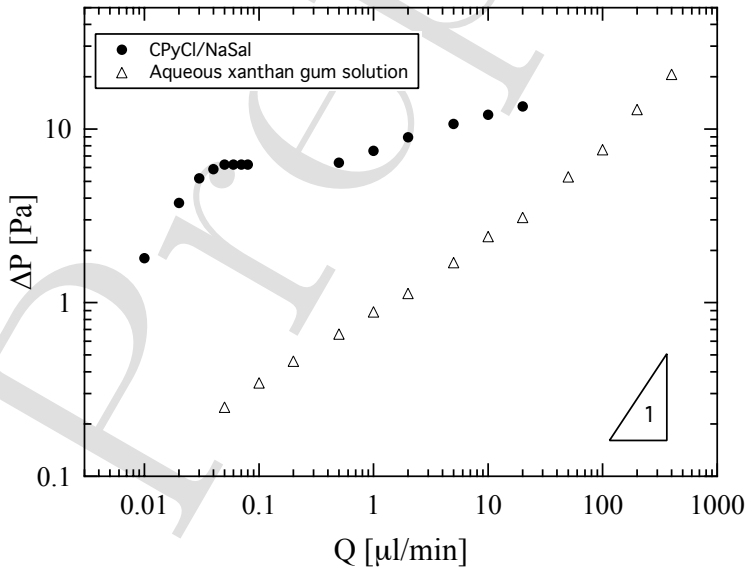


**Fig. 14** Pressure drop $\Delta P$ versus flow rate $Q$ for the CPyCl/NaSal micellar fluid and the xanthan gum solution measured using VROC channel A.

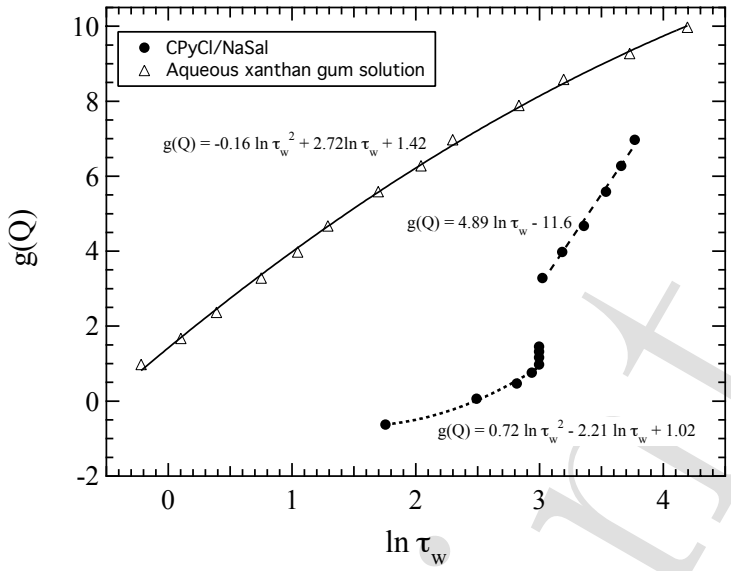


**Fig. 15** $g(Q) = \ln \dot{\gamma}_a$ versus $\ln \tau_w$ for CPyCl/NaSal and and xanthan gum solution (measured using VROC channel A). The polynomial functions fitted are given next to the data.

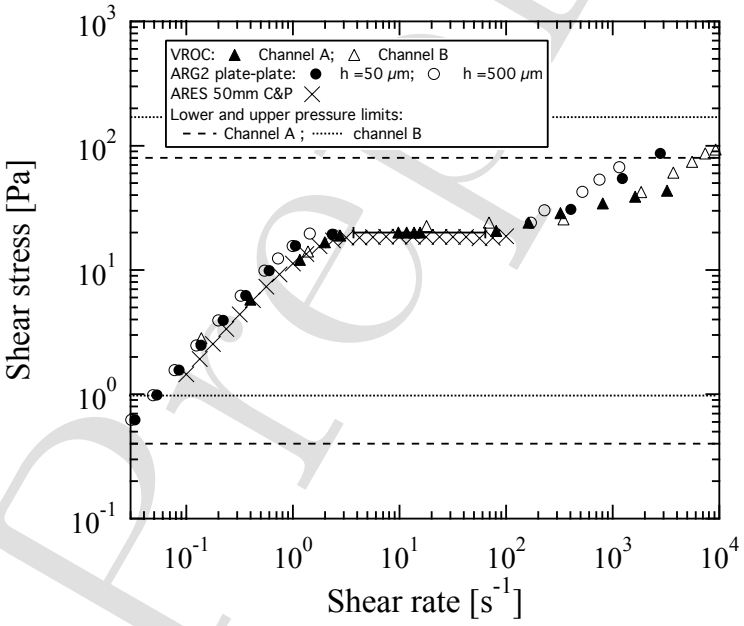


**Fig. 16** Flow curve for CPyCl/NaSal. The error bars for the VROC data in the stress plateau are discussed in the text.

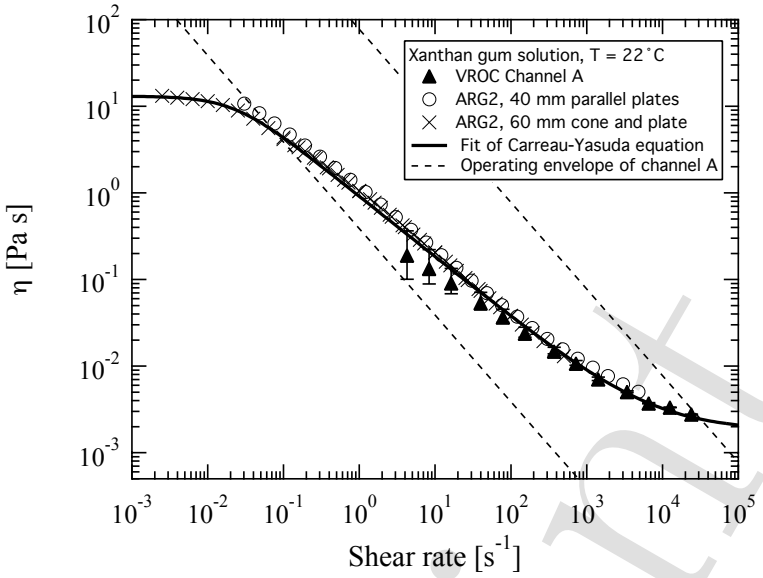


**Fig. 17** Viscosity as a function of shear rate for aqueous xanthan gum solution from $10^{-3} < \dot{\gamma} < 3 \times 10^4$ s$^{-1}$.

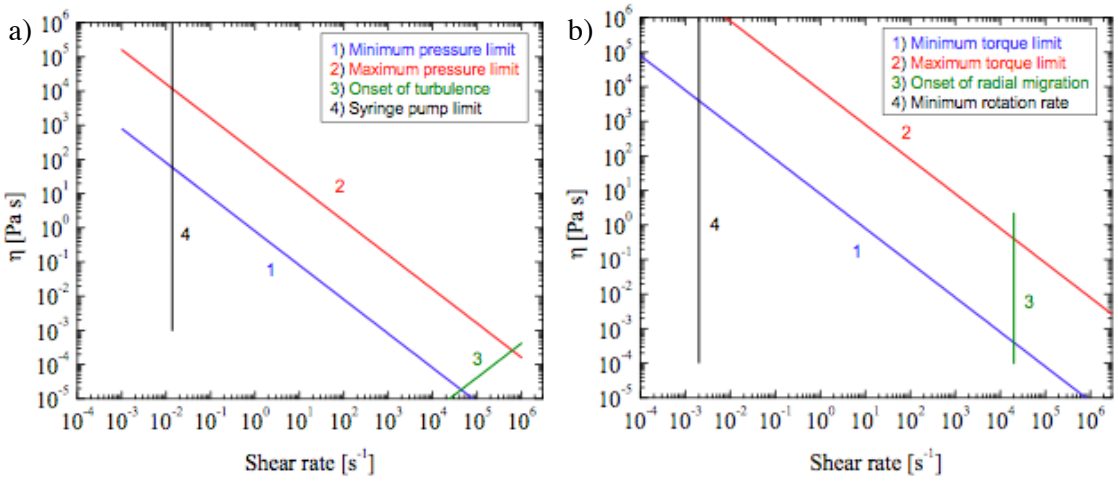


**Fig. 18** Operating region in the viscosity/shear-rate space for a microfluidic rheometer (VROC) and a strain-controlled rheometer (ARES). a) The operating region for VROC channel B. The lines labeled 1, and 2 of slope -1 are the limiting curves based on the minimum and the maximum measurable pressure difference $\Delta$P (Eqs. 8, 9). Line 3 is based on the shear rate – viscosity cutoff at which the flow approaches a Reynolds number $Re = 2000$, and can become turbulent. The vertical line 4 is a low shear rate cutoff ($\dot{\gamma} = 0.0132\ \text{s}^{-1}$) based on the minimum flow rate achievable. b) Equivalent operating space for a strain controlled rheometer (ARES). The lines 1 and 2 are the limiting curves based on the minimum and the maximum measurable torque (Eq. 15). The vertical line 3 is the high shear rate cutoff ($\dot{\gamma} = 2 \times 10^4\ \text{s}^{-1}$) for the onset of radial migration and viscous heating at a typical gap setting ($H = 50\ \mu$m). The vertical line 4 is the low shear rate cutoff ($\dot{\gamma} = 0.002\ \text{s}^{-1}$) based on the minimum controllable rotation rate of the fixture.